Determining Surface Roughness Using Extreme Ultraviolet Light

Joshua Marx

A senior thesis submitted to the faculty of
Brigham Young University
in partial fulfillment of the requirements for the degree of

Bachelor of Science

R. Steven Turley, Advisor

Department of Physics and Astronomy

Brigham Young University

April 2014

Copyright © 2014 Joshua Marx

All Rights Reserved

ABSTRACT

Determining Surface Roughness Using Extreme Ultraviolet Light

Joshua Marx
Department of Physics and Astronomy
Bachelor of Science

I used extreme ultraviolet light to find the surface roughness of three Uranium Oxide thin films of approximate thicknesses 140 nm, 114 nm, and 40-45 nm. The wafers were first scanned to measure the non-specular reflectance of each sample. I combined the scans with the same angle of incidence, and then normalized the combined data to calculate the reflectance per unit angle using diffuse reflection. Next, I compared the data to Huygens' and geometrical optics calculations to estimate surface RMS height and the spatial frequency distribution. I have also compared the roughness height and frequency distribution to measurements taken on the SEM. By comparing our non-specular curves to geometrical optics, Huygens' calculations and physical measurements we are able to create a model accurate enough to describe the non-specular scattering from surfaces with roughness having spatial frequencies much less than one over the wavelength. Our research group hopes to be able to use this data make smoother samples in the future and find new and better ways to model thin film surfaces.

Keywords: surface roughness, extreme ultraviolet light, thin films, uranium oxide, geometrical optics, Huygens' method, ALS

ACKNOWLEDGMENTS

I would like to thank Steve Turley for all his help. He has been instrumental in my physics career and has helped me find real world applications to my classroom learning. He is one of the smartest men I know and is always willing to help, even when it is inconvenient. None of this would have been possible without the help of Steve Turley; this thesis is dedicated to him. I would also like to thank David Allred for his support of my project and for providing us with the thin films that we have experimented on. I am extremely grateful to Dr. Eric Gullikson and the other staff at the Advanced Light Source at the Lawrence Berkeley National Lab, particularly those responsible for Beamline 6.3.2, for their support as we took measurements. Finally, I would like to show my love and appreciation for my family and all the support they have given me over the years. They have been with me through the whole process and I could not have done it without them. Thanks to everyone who has been there for me.

Contents

Table of Contents iv

List of Figures v

1 Introduction 1
- 1.1 Extreme Ultraviolet Light 1
- 1.2 Surface Roughness 3
- 1.3 Thin Films 6
- 1.4 Current Roughness Measurements 7
- 1.5 Calculating Reflectance 10

2 Experimental Methods and Calculations 14
- 2.1 Our Thin Films 14
- 2.2 Advanced Light Source 15
- 2.3 Mathematical Analysis 22

3 Results and Analysis 28
- 3.1 Introduction 28
- 3.2 Huygens' Calculations 28
- 3.3 Determining Surface Roughness 34
- 3.4 Future Work 51

A Mathematica Code 52

B Graphs 53

Bibliography 59

List of Figures

1.1 Specular reflection 4

1.2 Non-specular reflection 5

1.3 Surfaces with differing spatial frequencies 5

1.4 Mulitlayer reflection 6

1.5 Representation of an AFM tip being dragged across a surface that has roughness with a high spatial frequency 8

1.6 Graph showing how an AFM can produce an inaccurate profile 8

1.7 Sample preparation for a TEM 9

2.1 Side view of a sputtering chamber. 15

2.2 A holder at the ALS containing a variety of thin films 17

2.3 The chamber at the ALS where we placed the holder and performed the scans . . . 18

2.4 Diagram of incidence and reflected beams 19

2.5 Schematic of a photodiode 20

2.6 Dark current for 5 nm light 21

2.7 Dark current for 15 nm light 22

2.8 Schematic for Beamline 6.3.2 at the Advanced Light Source 23

3.1 Reflection from a flat surface using Huygens calculations 29

3.2 Reflection from a long flat surface using Huygens calculations 30
3.3 Two different surfaces that have the same RMS height and spatial frequency parameters 31
3.4 Reflection from two different surfaces that have the same RMS height and spatial frequency parameters 32
3.5 Two different surfaces that have the same RMS height but different spatial frequency parameters 32
3.6 Reflection from two different surfaces that have the same RMS height but different spatial frequency parameters 33
3.7 Two different surfaces that have different RMS heights but the same spatial frequency parameters 33
3.8 Reflection from two different surfaces that have different RMS heights but the same spatial frequency parameters 34
3.9 Reflection per unit angle for uranium oxide sample 1 at 2.5 nm with a fixed incidence angle of 2.5 degrees 35
3.10 Histogram of reflected rays 36
3.11 Model of the surface of uranium oxide sample 1 37
3.12 Histogram of the rays reflecting from uranium oxide sample 1 37
3.13 Scan taken by an SEM of uranium oxide sample 1 38
3.14 Reflection per unit angle for uranium oxide sample 2 at 2.5 nm with a fixed incidence angle of 2.5 degrees 39
3.15 Model of the surface of uranium oxide sample 2 40
3.16 Histogram of the rays reflecting from uranium oxide sample 2 40
3.17 Reflection per unit angle for uranium oxide sample 3 at 15 nm with a fixed incidence angle of 10 degrees 41

3.18 Model of the surface of uranium oxide sample 3 42
3.19 Histogram of the rays reflecting from uranium oxide sample 3 42
3.20 Reflection per unit angle for uranium oxide sample 1 at 15 nm with a fixed incidence angle of 10 degrees 43
3.21 Reflection per unit angle for uranium oxide sample 1 at 15 nm with a fixed incidence angle of 10 degrees without error bars 44
3.22 Computed reflection using Huygens' method for uranium oxide sample 1 at 15 nm with a fixed incidence angle of 10 degrees 45
3.23 Surface found using Huygens' program 45
3.24 Reflection per unit angle for uranium oxide sample 1 at 15 nm with a fixed incidence angle of 10 degrees, shown on a linear scale 46
3.25 Computed reflection using Huygens' method for the non-specular portion of uranium oxide sample 1 at 15 nm with a fixed incidence angle of 10 degrees 47
3.26 Theoretical surface found using Huygens' program 47
3.27 Reflection per unit angle for uranium oxide sample 2 at 15 nm with a fixed incidence angle of 10 degrees 48
3.28 Theoretical surface found using Huygens' program 49
3.29 Computed reflection using Huygens' method for uranium oxide sample 2 at 15 nm with a fixed incidence angle of 10 degrees 50
3.30 Reflection per unit angle for uranium oxide sample 2 at 15 nm with a fixed incidence angle of 10 degrees, shown on a linear scale 50

B.1 Reflection per unit angle for uranium oxide sample 1 at 5 nm with a fixed incidence angle of 3 degrees 53
B.2 Reflection per unit angle for uranium oxide sample 1 at 30.4 nm with a fixed incidence angle of 10 degrees 54

B.3 Reflection per unit angle for uranium oxide sample 2 at 5 nm with a fixed incidence angle of 3 degrees 55
B.4 Reflection per unit angle for uranium oxide sample 3 at 2.5 nm with a fixed incidence angle of 2.5 degrees 56
B.5 Reflection per unit angle for uranium oxide sample 3 at 5 nm with a fixed incidence angle of 4 degrees 57
B.6 Reflection per unit angle for uranium oxide sample 30 at 30.4 nm with a fixed incidence angle of 10 degrees 58

Chapter 1

Introduction

1.1 Extreme Ultraviolet Light

Extreme ultraviolet (XUV) light is light with wavelengths between one and 60 nanometers. The shorter wavelengths of light in this range are on the same order of magnitude as atomic dimensions. Currently, XUV optics have many uses and even more potential applications in a variety of fields, such as photolithography, plasma diagnostics, and astrophysics.

Currently, photolithography is used to fabricate circuits, and the circuit size is limited by the wavelength of light used. In order to make a smaller circuit, a smaller wavelength of light is required. Since XUV light has such small wavelengths, the next generation of nanoscale lithography may be using XUV light [1]. However, there needs to be advancements to the current XUV optics in order for XUV lithography to become a reality [2].

Extreme ultraviolet light is also used for measuring the blackbody temperature of plasmas. Those working with fusion reactors or nuclear weapons need to analyze and diagnose the plasma created, and they particularly investigate the temperature of the plasma. With blackbody radiation, the intensity is a function of wavelength, and has a peak in the XUV spectrum. In order to utilize

signals at these wavelengths they need to have optics capable of looking at XUV light.

Astrophysicists study all kinds of different objects, and each one radiates at a different frequency. By inspecting the different wavelengths given off, they can inspect different features of the object. To look at bodies that are brighter in the XUV, they need to have high quality XUV optics. By looking at all of these different applications, XUV optics are very important and will be crucial to advancing scientific progress.

The variety of uses makes XUV research very valuable; however, there are also many limitations associated with these wavelengths. One of the primary concerns is that XUV light has a large imaginary part in its index of refraction causing it to be strongly absorbed in nearly every material. Also, since the wavelengths of light in the XUV spectra are on the same order of magnitude as atomic spacing, the reflectance is extremely sensitive to aberrations on the surface or other forms of surface roughness. Such sensitivity means that any thin film used for reflection in the XUV must have its thickness controlled to within one nanometer while having an extremely smooth surface.

In order to understand why XUV light is absorbed so easily, one must understand how it interacts with materials. The index of refraction of a material is frequency dependent and is given by,

$$n = 1 - \delta + i\beta. \tag{1.1}$$

In Equation 1.1, 1-δ represents the real part and β the imaginary part of the index of refraction. This distinction becomes critical when working with XUV light, because in the XUV range both δ and β are close to zero for most materials. In the independent atom approximation, δ and β are proportional to the density of the material [3]. This becomes important when considering surface roughness later. These properties mean that most materials absorb most XUV light while reflecting back very little, as can be seen in the derivations below.

Reflection at normal incidence between vacuum and a bulk material is given by

$$r = \frac{n_1 - n_2}{n_1 + n_2}, \tag{1.2}$$

where n_1 = 1, or index of refraction of a vacuum, and $n_2 = 1 - \delta + i\beta$. For a mirror with multiple layers, the reflection from each layer must be added together in phase, see Fig. 1.4. Simplifying these equations gives

$$r = \frac{\delta - i\beta}{2 - \delta + i\beta}. \tag{1.3}$$

Since both δ and β are close to zero, the intensity of the reflected light is small in Eq. 1.3.

The problem of low reflectance is further compounded by how much of the light is absorbed. The equation for a plane wave is given by

$$e^{ikx} \tag{1.4}$$

where

$$k = \frac{2\pi n}{\lambda}. \tag{1.5}$$

Using the index of refraction for XUV light, Eq. 1.1, causes Equation 1.4 to simplify to

$$e^{-\frac{2\pi\beta}{\lambda}x}. \tag{1.6}$$

In order to see how quickly the light is absorbed, or the intensity attenuated to $1/e$, we set Equation 1.6 equal to e^{-1} and solve for x. We find that

$$x = \frac{\lambda}{2\pi\beta}. \tag{1.7}$$

A typical value for β in the XUV is between 0.1 and 0.2, in which case x is approximately equal to λ. This means that after the light has passed one wavelength into the material, it is already $1/e$ of its original intensity.

1.2 Surface Roughness

As explained above, most materials make poor reflectors of XUV light. This makes it crucial to maximize the possible reflection. In order to increase the amount of light reflected off of the

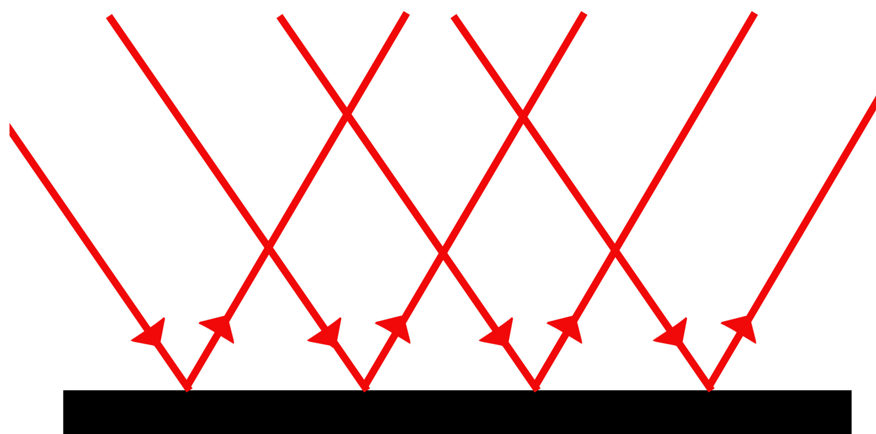

Figure 1.1 Specular reflection from a flat surface

sample, one must first decrease the amount of surface roughness, or the variations in surface height. This becomes especially relevant in the XUV as the wavelength of light can be on the same order of magnitude as the thin film surface roughness. Consequently roughness can have a considerable effect on XUV reflectance as can be seen in Fig. 1.2 as compared to Figure 1.1 [4, 5]. When a surface is perfectly flat and the beam is much larger than the wavelength, all light is reflected at the same angle creating specular reflection. As the size of the beam approaches the wavelength, there is also diffraction of the beam at the surface. This diffraction causes light to reflect off at non-specular angles but, in our case, this amount is small compared to the specular peak as is seen later with the Huygens' calculations. However, when the surface is rough, even a wide beam is reflected at a range of angles creating non-specular or diffuse reflection. This scattering decreases the intensity of the specular peak as energy must be conserved, meaning the scattered light has to come from the peak.

There are two kinds of surface roughness caused variation in composition and variation in surface height. The first kind is caused by different concentration and density of atoms at the surface and differing phases across the surface of the material. This produces an index of refraction that is a function of position, $n(z)$. Variation in surface height can also be classified in two separate

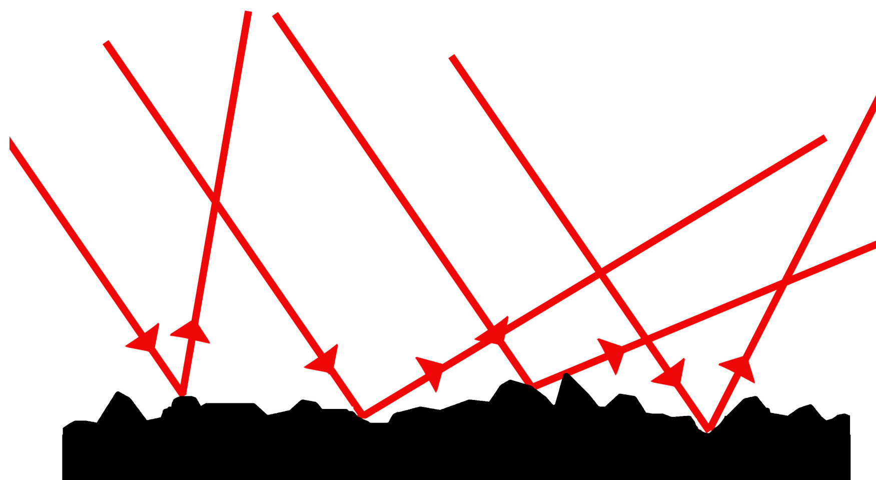

Figure 1.2 Diffuse reflection from a rough surface

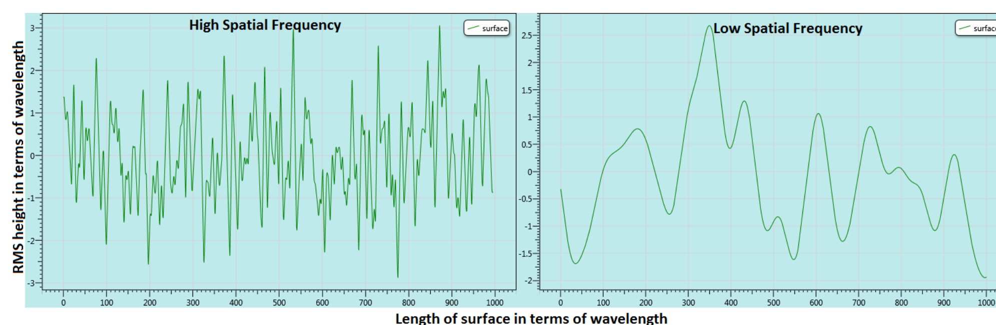

Figure 1.3 High vs. low frequency roughness

ways. The first is root mean square, RMS, height which is a measurement of the average deviation of the thin film from a perfectly flat plane. The second characteristic is spatial frequency, or how the peaks are distributed. Peaks far from each other have a low spatial frequency while surfaces with close peaks have a high spatial frequency as seen in Fig. 1.3. In order to calculate the surface roughness of a sample, we need to know the RMS height and how the roughness is distributed.

It is important to note that Stearns shows that the same treatment can be used when considering the two different kinds of surface roughness [5]. In his paper, Stearns shows how to analytically account for scattering of XUV light due to roughness [5]. While his work is extensive, he makes certain approximations that are not valid in our situation, namely that the surface must have a low

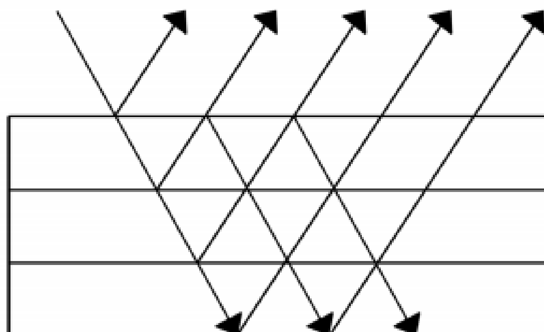

Figure 1.4 Reflection from a multilayer mirror. If all the layers thicknesses are precisely controlled, then each layer contributes to the total reflection.

variations in surface height and a low reflectance [5]. In our research some of our thin films have RMS roughnesses on the same order of magnitude as the shortest XUV wavelengths.

1.3 Thin Films

To further research the effects of XUV light, our research group has made thin films from various materials that we have tested to see how rough the surfaces are. These materials include thorium, ruthenium, aluminum, uranium, yttrium and silicon nitride. These optics need to be created with very precise specification of layer thickness and roughness in order to reflect as much XUV light as possible. Many of the thin films are multilayer mirrors which create a composite reflectance in the XUV. For these to work properly, each layer thickness must be controlled to less than one nanometer so that the reflected beams from each layer add constructively, as seen in Fig. 1.4.

Another crucial aspect of our thin films is the index of refraction. Not all indices of refraction for materials are well known in XUV, particulary when oxidation, hydration, and phase changes are taken into account. Due to these effects, we do not always know the index of refraction and would like to account for it. To calculate it, we need to understand the layers' roughness to form an accurate fit. All of these reasons make it crucial that we know how rough the surface of the

sample.

1.4 Current Roughness Measurements

We need to be able to resolve features that are smaller than the shortest XUV wavelengths. This is crucial as features of this size and larger affect the reflectance we see from the surface. While there are currently many ways of determining the height of the of thin film surfaces, most cannot reach this precision. Currently, Atomic Force Microscopes (AFM's), electron microscopes, and ellipsometry are used to image the surface and to determine the thickness of the various layers of the thin films. While these techniques are popular, they have many detriments that prevent them for being as precise as we require.

Right now, the best way to measure surface roughness is using an AFM. An AFM functions by dragging, or bouncing, a small tip across the surface. The tip is attached to a cantilever and a laser reflects from the end of the cantilever. This laser records the movement up and down of the tip, which then maps out the profile of the surface. This technique excels when the spatial frequency of the surface roughness is between the radius of the tip and one micron. However, the AFM tip has a non-zero width that cannot measure the entire RMS height when the spatial frequency is smaller than the width, see Figure 1.5 [6]. This can be seen in Figure 1.6 as the AFM measure an RMS roughness of 2.3 Angstroms rather than actual value of 10.3 Angstroms [6]. This shows that while AFM's can be used for some samples, they cannot map small surface variations.

Another common method is to measure the surface roughness using electron microscopes. Scanning Electron Microscopes (SEM's) focus a narrow beam of electrons onto the surface and then scan this beam across the surface, much like the AFM rasters the tip back and forth. One again the problem is that an SEM cannot always pick up the fine details that are requisite to image the surface at the magnitude desired, as the wavelength of the electron beam is larger than the fea-

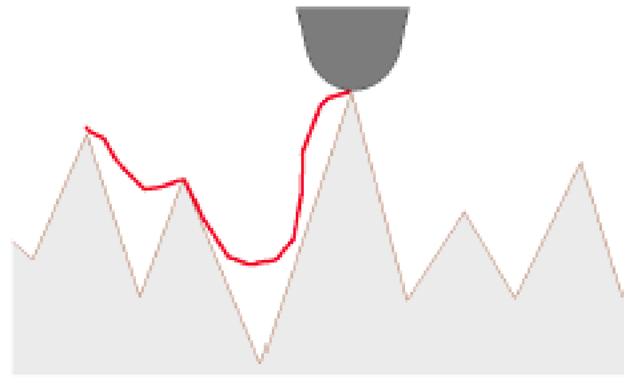

Figure 1.5 If the surface has roughness with a high spatial frequency, then the tip cannot produce an accurate profile of the surface [6].

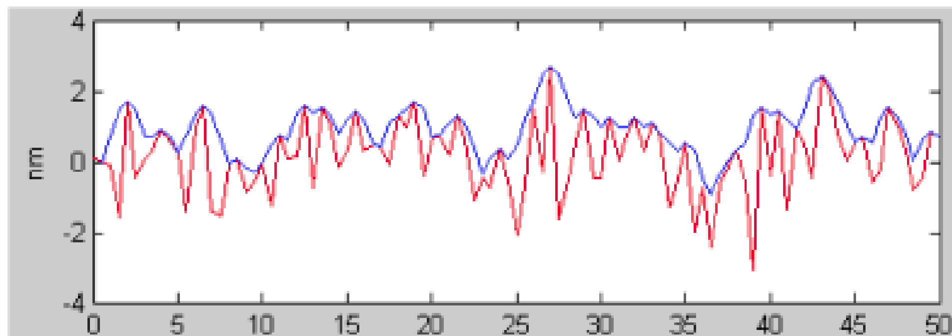

Figure 1.6 The red line shows a model surface, however the AFM tip detects a surface profile shown by the blue line. This is because the tip has a finite width that does not allow it to map all of the surface contours. The actual RMS roughness of the surface is 10.3 Angstroms, but the AFM reports an RMS roughness of 2.3 Angstroms [6].

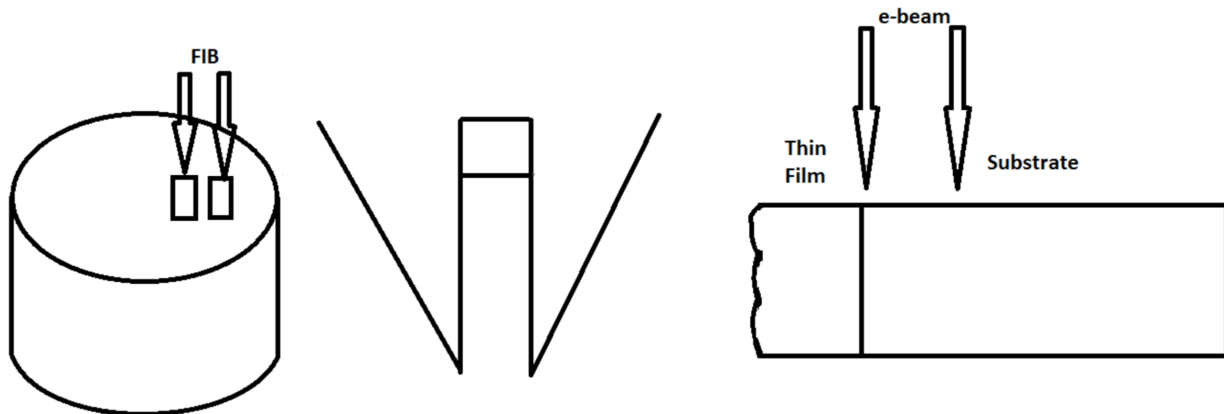

Figure 1.7 Samples used on a TEM need to be thin, usually between 10-100 nm thick. Due to this restriction, most imaging of thin films are done by imaging a cross section of the sample. A focused ion beam is used to cut away two wedges on a sample, leaving the thin film and the substrate. This is shown in the left and center picture as a top view and cross section view of the process. This thin slice of the sample is then removed, and the profile of it is imaged on the TEM. This allows a view of the interface between the thin film and the substrate, but does not allow a clear view of the RMS surface roughness.

tures we are inspecting. The other electron microscope is the Transmission Electron Microscopes (TEM's) which requires difficult sample preparation. The TEM can only be used on extremely thin samples, typically between 10-100 nm, so normally only a profile of a thin film is imaged, as shown in Fig. 1.7. In order to obtain the TEM sample, a focused ion beam is used to cut away two wedges on a sample, leaving the thin film and the substrate. This is shown in the left and center picture of Fig. 1.7 as a top view and cross section view of the process. This thin slice of the sample is then removed, and the profile of it is imaged on the TEM. This allows for close examination of the interface of different layers, but is impractical for measuring roughness. In creating these thin samples, the material we are trying to profile is invariably damaged making the imaging even less useful .

1.5 Calculating Reflectance

To improve upon other methods we are working on finding a new way to map surface roughness using non-specular reflectance. This method analyzes the intensity of light that reflects off at different angles from a set portion of the sample, and calculates the reflectance per unit angle at the specific wavelength. To accomplish this, we went to the Advanced Light Source (ALS) at the Lawrence Berkeley National Labs (LBNL) and took non-specular reflectance scans of the surfaces of our wafers. We then took this data and computed the reflectance per unit angle of the samples in order to map the surfaces of the optics.

The results from the ALS can be compared to different optical methods to determine variations of surface height, however only geometric optics and Huygens' calculations will be used in the calculation of this data. The first way is Physical optics (PO) calculations. Physical optics calculations are completed using a number of steps outlined below. Physical optics calculations give us a reflectance curve that we can then compare to our results from the ALS. This method gives more accurate comparisons to thin films with low surface roughness.

1. Assume an incident plane wave interacts with the surface.

2. The surface current at each point is estimated using Kirchhoff's approximation. This method involves approximating the current on the surface as the one which would be induced on a plane tangent to the surface at that point. The current is calculated using Fresnel coefficients and applying the boundary conditions inferred from Maxwell's equations. The Kirchhoff approximation assumes that the spatial frequency components of the surface are small compared to one over the wavelength and that the RMS roughness is small compared to the wavelength. Then the surface is approximately locally planar over a region that is several wavelengths in size.

3. After finding the surface currents, they are used as sources of radiated fields using Maxwell's

equations. We then use these radiated field to calculate the reflectance per unit angle.

Another method is to use Huygens' principle. This method samples the surface over a series of equally spaced points. It assumes that current on the surface is constant in a region centered around each point. The phase of the current is equal to the phase of an incident plane wave with an amplitude of one. The integral of the current density is accomplished by summing the currents from each point. For our calculations we only considered a single layer surface and so only took the part of the beam being reflected, and ignored the transmitted portion. A limitation of this method is it considers all of the radiated fields as being of equal amplitude independent of the index of refraction or incidence angle. Also, as we increase the number of surface points to approach the nominal surface height, Huygens' scattering density increases. This can be approximated as an increasing index of refraction as a function of surface height which is directly related to interfacial roughness discussed earlier. As the density of the material increases, so do δ and β.

Huygens' principle differs from PO calculations in two main ways. The first is that the Huygens' method replaces the high order integration used in PO with a low order technique. This requires the Huygens' method to use more points to get the same accuracy. The other is that PO takes into account the varying index of refraction of thin films using Fresnel coefficients. This allows it to vary the reflectance of different indices of refraction and different angles of incidence. Huygens' method assumes perfect reflection, or, in PO terms, reflection from a perfect conductor.

Despite these limitations, Huygens' method still gives useful insights. Results from our PO calculations show that first order effect of changing the index of refraction from that of a perfect to imperfect conductor is to change the overall amplitude of the reflectance. It does not significantly affect the relative amplitude or scattering pattern of the non-specular reflectance. This allows us to use Huygens' method for an approximation of the scattering pattern. Huygens' calculations also take into account diffraction effects from the beam. We can see how diffraction effects dominate the non-specular scattering when the RMS roughness is low. At higher RMS roughnesses, the

scattering from surface roughness effects dominate the diffraction effects. Using Huygens' method we can create a model accurate enough to describe the non-specular scattering from surfaces with roughness having spatial frequencies much less than one over the wavelength.

To compute the reflectance using Huygens' method, Steve Turley wrote a program that I used during my analysis. The program uses a uniform random number generator to create a surface so that the amplitude at each point has an equal probability of being between -1 and 1. This is done in the Fourier domain so this is the amplitude of the Fourier component. We then multiply by a half-Gaussian of a desired width to attenuate the amplitude of different random frequency components; this biases the surface to favor the lower spatial frequencies. We take the inverse Fourier transform of the amplitude components to put it in the spatial domain. We now compute the RMS roughness of the created surface. To obtain a surface with a specific desired RMS height, we multiply the surface by the desired RMS height over the computed RMS roughness. This allows us to vary the spatial frequency components and the RMS height to create a model surface from which we can calculate the reflectance. Each run creates a new surface that has the same Gaussian envelope but different random amplitudes for the spatial frequency components. This is important because we can average the computed reflectance to find how a class of mirrors work, rather than one point on one particular surface.

The final method used to calculate reflection from a surface is geometrical optics, which is also called ray tracing. This is the simplest method, but also has a limitation that feature size causing the reflection must be much larger than the wavelength. This method applies Snell's law at the surface to calculate the angle of reflection. We used this method when the surfaces created using Huygens' method do not match the reflectance from our samples in order to find an approximation of the surface. This method will then be later used to create a better surface model then the one currently used.

Our research group has gone beyond the assumptions inherent with PO and Huygens' principle

by solving Maxwell's equations using a boundary element method [6]. Rather than finding surface currents at a plane tangent to the surface, this numerical method finds what the actual current density would be. These calculations show that PO and Huygens' calculations are acceptable under the conditions outline in the previous paragraphs [6,7]. They are insufficiently accurate with the spatial frequencies have significant components larger than one over the wavelength or when the RMS surface height is on the order of magnitude or larger than the wavelength.

Chapter 2

Experimental Methods and Calculations

2.1 Our Thin Films

David Allred has sputtered numerous thin films made of different materials including uranium oxide (UOx), yttrium oxide (YO) and silicon nitride (SiNx). The films made from UOx and SiNx were formed using DC sputtering while the YO samples were made using RF sputtering. These samples are of various thicknesses and are made for XUV optics. However, the variation in surface roughness is unknown making an accurate analysis of the index of refraction impossible.

My research focuses on three uranium oxide thin films with varying degrees of roughness. These were made using DC magnetron sputtering (DCMS). Sputtering must always be done in a vacuum, so the wafers are placed in a chamber which is then pumped down to high vacuum. Argon is then flowed into the chamber and a DC voltage is added that creates an argon plasma. Bell further describes the process which we use in our lab in his thesis, and a schematic of the sputtering chamber can be see in Figure 2.1 [8]. As can be seen, a magnet behind the target confines the plasma above the target, and an electric field accelerates the argon ions toward the target. In our case the target is the uranium and the argon atoms collide with the uranium and

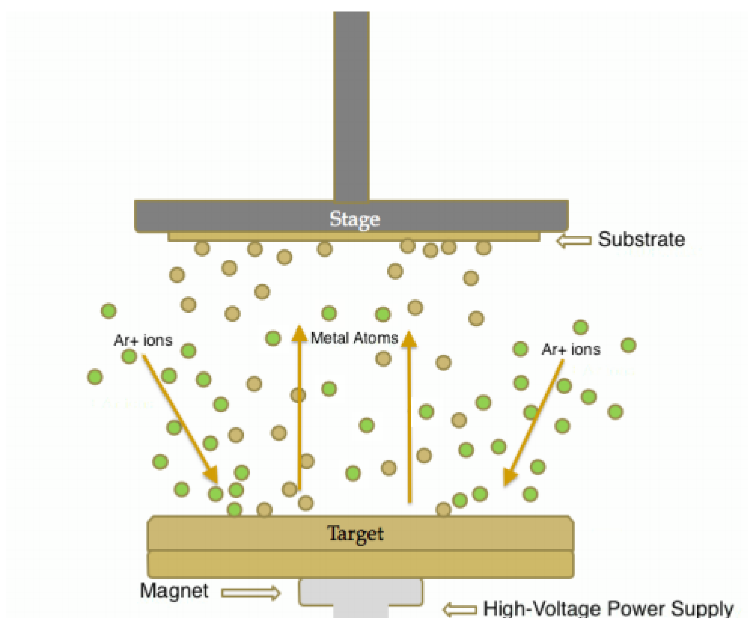

Figure 2.1 Side view of a sputtering chamber. The substrate can be seen at the top of the diagram, with the uranium target at the bottom. The uranium atoms are sputtered off the target and then stick to the substrate to form the thin film.

sputter off atoms. These sputtered atoms are focused in a cylinder above the target by the magnetic field so that they hit the substrate and form a thin layer of uranium on the silicon wafer. The uranium is partially oxidized during flight by residual oxygen in the chamber and also undergoes natural oxidization after the sputtering process. We do not know the exact stoichiometry for our uranium oxide thin films.

2.2 Advanced Light Source

We measured the reflectance per unit angle of our samples at the ALS at the LBNL where we took non-specular reflectance measurements. We received an allocation for beam time on Beamline 6.3.2. Beamline 6.3.2 is dedicated to experiments involving XUV light, and its schematic can be seen in Figure 2.8. The photons on this beamline have an energy range from 25-1300 eV [9]. This is important as it allows us to measure our samples at a variety of wavelengths while still

maintaining a high intensity. The beam itself has a spot size of 300 x 100 μm at the surface of the sample, the 300 μm is in the perpendicular direction with respect to the direction the angles were measured [9].

We took our scans by placing our samples on a holder and pumping down the chamber to high vacuum, less than one milliTorr. The holder can be seen in Fig. 2.2 and the chamber in Fig. 2.3. The holder in the picture has samples of uranium oxide, yttrium oxide, and silicon nitride, but this paper is only addressing the uranium oxide thin films. We rastered the incident beam across the surface in a variety of locations in order to find a smooth and a rough spot so that we had measurements of the two extremes of surface roughness. Once we had chosen a spot, we set our sample to fixed angles with respect to the incident beam and reflected the beam off our sample to the detector. We then scanned the detector over a variety of angles to map the entire reflectance curve. Depending on the sample, we set the angles to 2.5, 3.0, 4.0, ,10.0, and 30.0 degrees. We also used an incident beam of 2.5, 5.0, 15.0, 25.0, and 30.4 nm light.

In order to properly calibrate the system, we had to make sure that the sample holder was properly positioned. If it was out of alignment, as we rotated the angle the beam would be reflecting off a different spot. As seen in Figure 2.3, the beam enters from the left of the chamber to interact with the detectors on the right side. In this set up, the z-direction is perpendicular to the target surface. To calibrate z properly we shined the beam directly into the photodiode and scanned the z direction from under the beam to above it. Using this scan we found where it bisected the beam and set this to 0. Next, we held the sample to a fixed angle and scanned the detector to find the specular peak. If the sample is at angle θ with respect to the incoming beam, then the specular peak should be at 2θ as seen in Figure 2.4. Using these scans we adjusted the θ_0 accordingly. After we adjusted the angle measurements we were aligned to within $1/10$ of a millimeter and $1/10$ of a degree.

The diffuse reflection scans were taken using two different detectors, a photodiode and a chan-

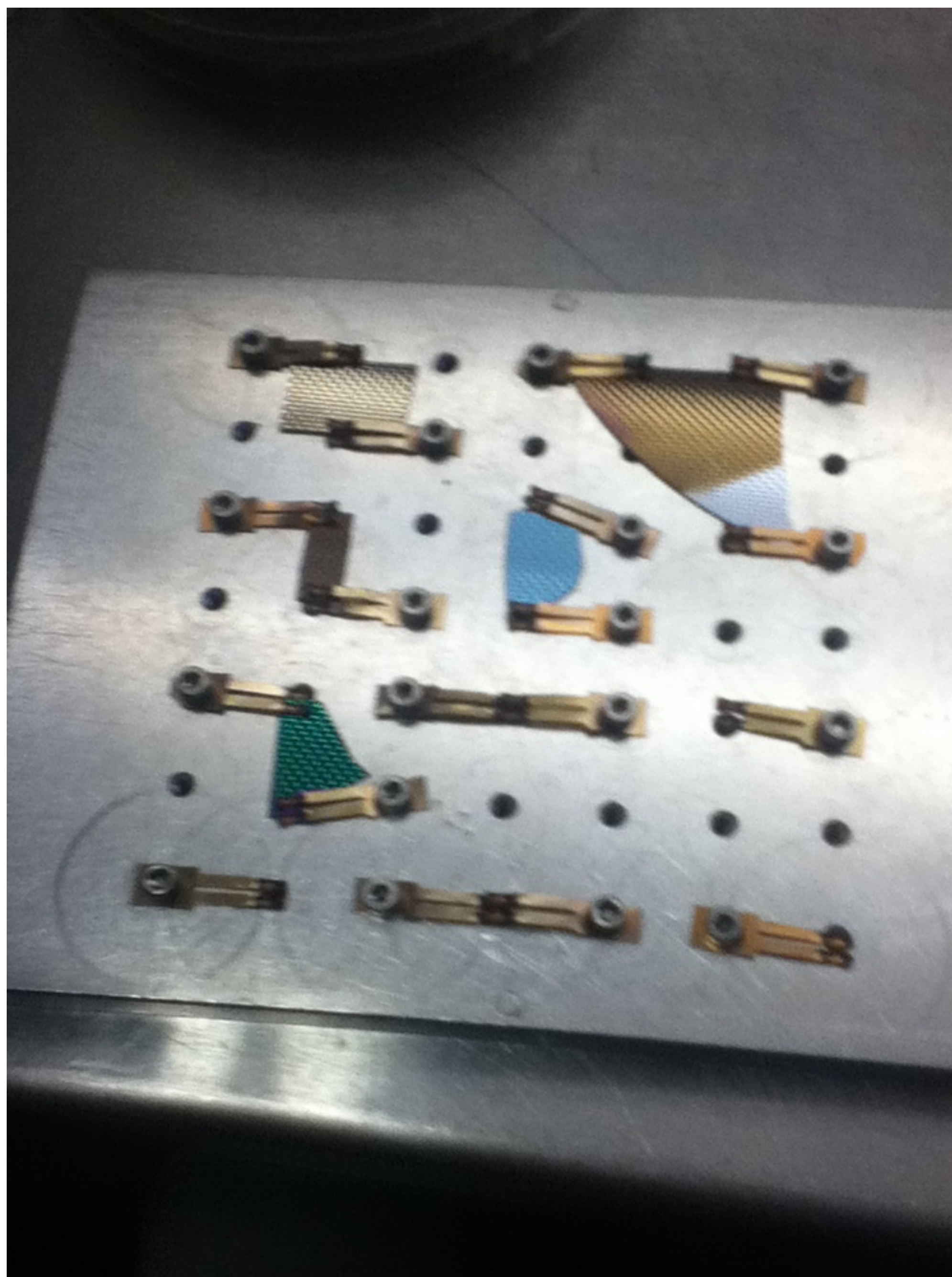

Figure 2.2 A holder at the ALS containing thin films made from uranium oxide, yttrium oxide, and silicon nitride. This thesis only treats the scans performed on the uranium oxide samples. For an indication of size, the distance between the different screw holes is one inch.

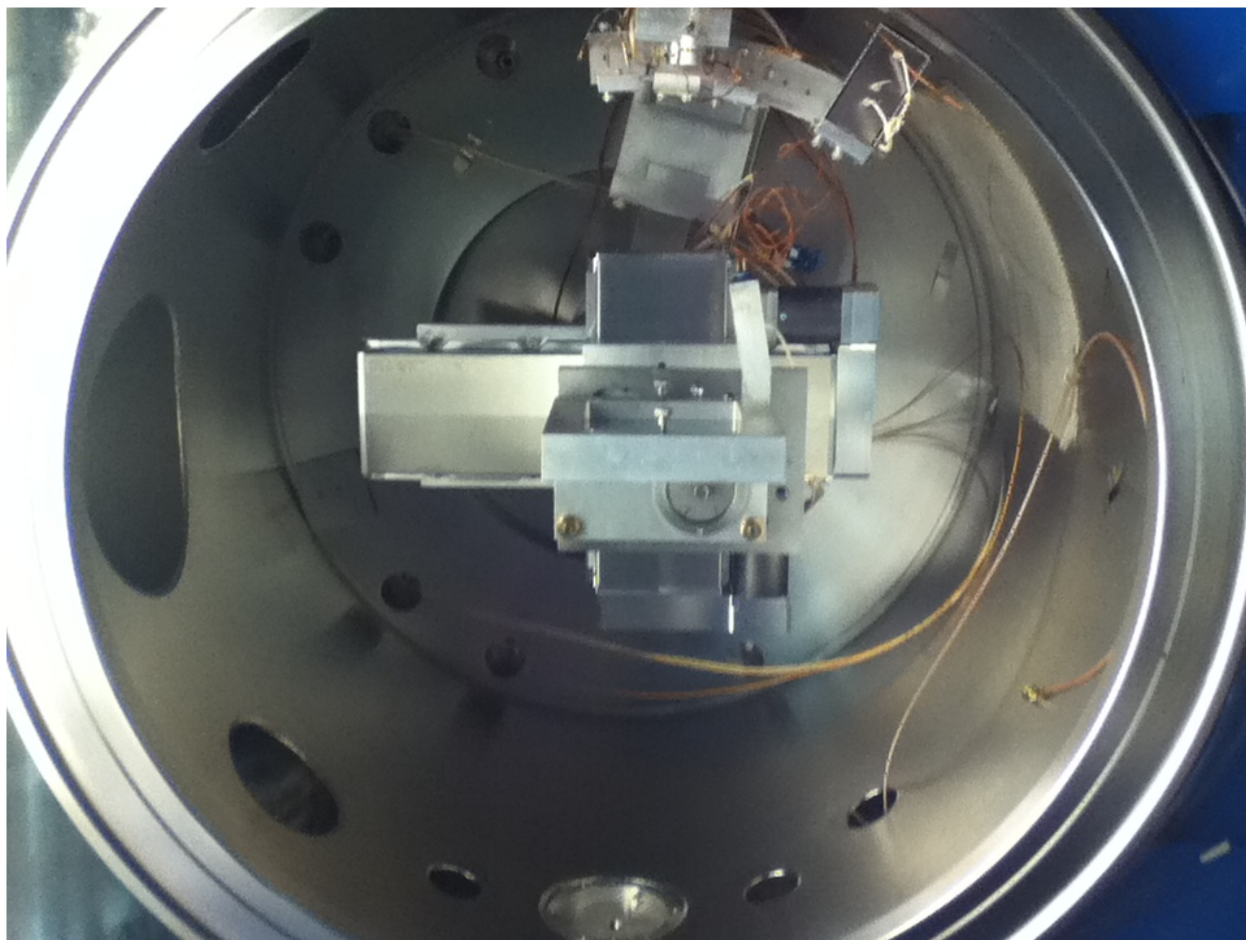

Figure 2.3 The chamber at the ALS where we placed the holder and performed the scans. The holder is placed in the middle. The different detectors are situated on the right side of the chamber. The incident beam comes in from the right.

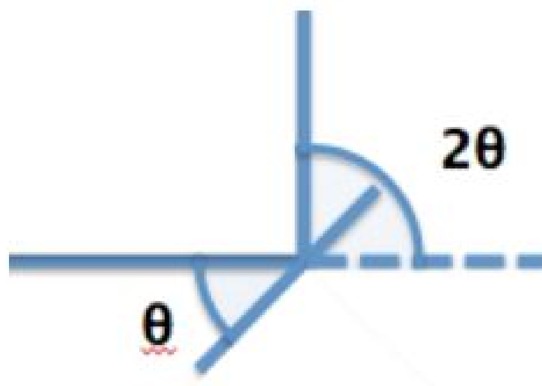

Figure 2.4 If the sample is at angle θ with respect to the incoming beam, then the specular peak should be at 2θ

nel electron multiplier (CEM)(also called a channeltron). A schematic for the photodiode circuit can be seen in Figure 2.5. The photodiode has a p-n junction. As the photons interact with the electrons and holes at the junction they produce a current that is proportional to the intensity of the light striking the detector. The current is sent through a current amplifier. Here the gain can be set to 10^7 to 10^{10}. In a real system, increasing the amplifier gain by a factor of 10 would not necessarily increase the signal by exactly the same factor. This uncertainty is a systematic error in the data that is not included in the quoted error bars. Once the signal is stepped up it passes through an analog to digital converter and the digital signal is sent to a computer. A photodiode is easy to use and is versatile, but it also has many limitations. One benefit of a photodiode is that it has no high end of range; if the signal gets to high we can decrease the gain in the current amplifier. However, it has a hard time picking up low intensities. At the lower ranges of intensity, the signal is on the same order of magnitude as the noise in the system, so amplifying the signal merely amplifies the noise along with it. While we were able to calibrate the angle and z direction in the system, we could not calibrate the gains. The gains, therefore, may not be exact so each gain may not be exactly $10x$ the previous gain.

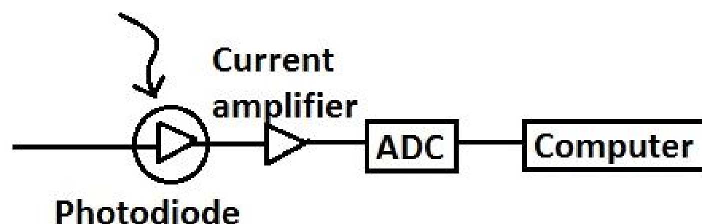

Figure 2.5 Schematic of a photodiode. Light strikes a photodiode generating a current. This current then passes through an amplifier that steps up the current by a certain gain. Next the signal passes through an analog to digital converter and the resulting signal is read by the computer.

The CEM can determine the number of photons striking the detector giving a much more accurate reading at low intensities. This also means that the detector can be easily saturated, and therefore damaged, by too intense of a beam. These restrictions caused us to measure the specular peak using the photodiode with a low gain, and then increase the gain as we scanned the increasing angles. We then switched detectors to the CEM find the reflectance of the wings of the non-specular reflectance curve. The CEM is very useful for taking readings using XUV light, because it is solar blind. A channeltron has photoelectric material with a work function higher than the energy of visible light. This means it is insensitive to ambient light and has a lower noise ratio, meaning there is not as much dark current.

Dark current is, in general, noise in the system. This noise can have a variety of causes, but it must be taken into account in order to properly ascertain a signal. Some dark current is from noise in the connection wires of the system. Dark current is more prevalent in a photodiode as there is also residual current in the amplifier and in the photodiode itself; the dark current for a CEM was found to be about 2-5 counts per minute, or relatively nonexistent. A photodiode is sensitive to all wavelengths of light, so any light leaking into the system can trigger a signal. It is also used at room temperature and is subject to thermal effects; the dark current is also temperature sensitive. The noise associated with dark current becomes especially significant when we use a large gain

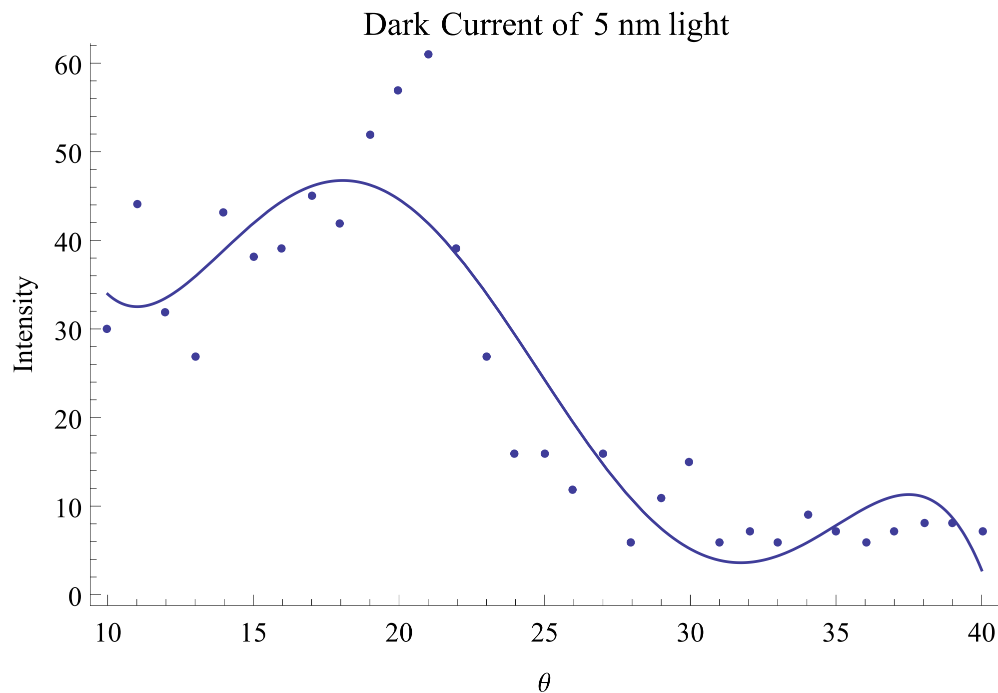

Figure 2.6 Graph showing how dark current varies with angle and is more sensitive to certain wavelengths as can be seen when compared to Fig. 2.7.

and have a low signal, as the noise is also amplified creating a high noise to signal ration. In order to account for dark current, we took numerous dark current scans. We would block the incidence beam and then see how much noise was in the system. We took dark current scans over time and across different detector angles, as well as at different wavelengths. This allowed us to see which angles and wavelengths were more prone to be noisy. As can be seen in Fig. 2.6 and 2.7, the noise is indeed dependent upon angle and certain wavelengths are more sensitive to dark current. We then were able to remove this noise from the true signal during our later calculations.

The CEM can become damaged if the beam is too intense. To attenuate the intensity properly, we had to place a variety of filters and pinholes in front of the beam to cut down the intensity. The filters were used to reduce the intensity as well, by passing the light through thin sheets of metal before the beam was picked up by the detector. Our analysis will have to take this into account as we calculate the reflectance for different wavelengths of light. We take similar scans using our

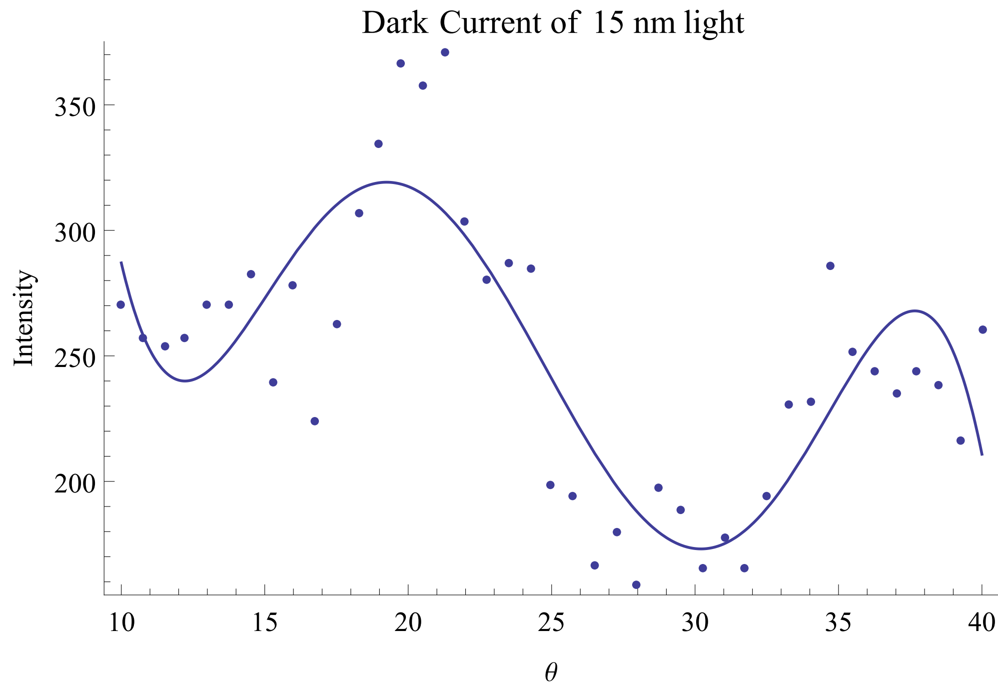

Figure 2.7 Graph showing how dark current varies with angle and is more sensitive to certain wavelengths as can be seen when compared to Fig. 2.6.

system at BYU, so we hope to be able to compare this data to scans taken in our research lab to see how accurate our system is.

2.3 Mathematical Analysis

The scans were taken using a variety of gains as we varied the detector angle away from the specular peak. We also placed a slit on the detector that was 1.29 cm by 0.05 cm. The purpose of the slit is t decrease the angular acceptance of the detector making the measurements more precise. These different runs needed to be joined together and put on the same scale to compensate for the different gains. The combined curve was an equivalent reflectance curve as if all the data were taken with the same detector, filter, and gain. This reflectance curve was formed using the following steps:

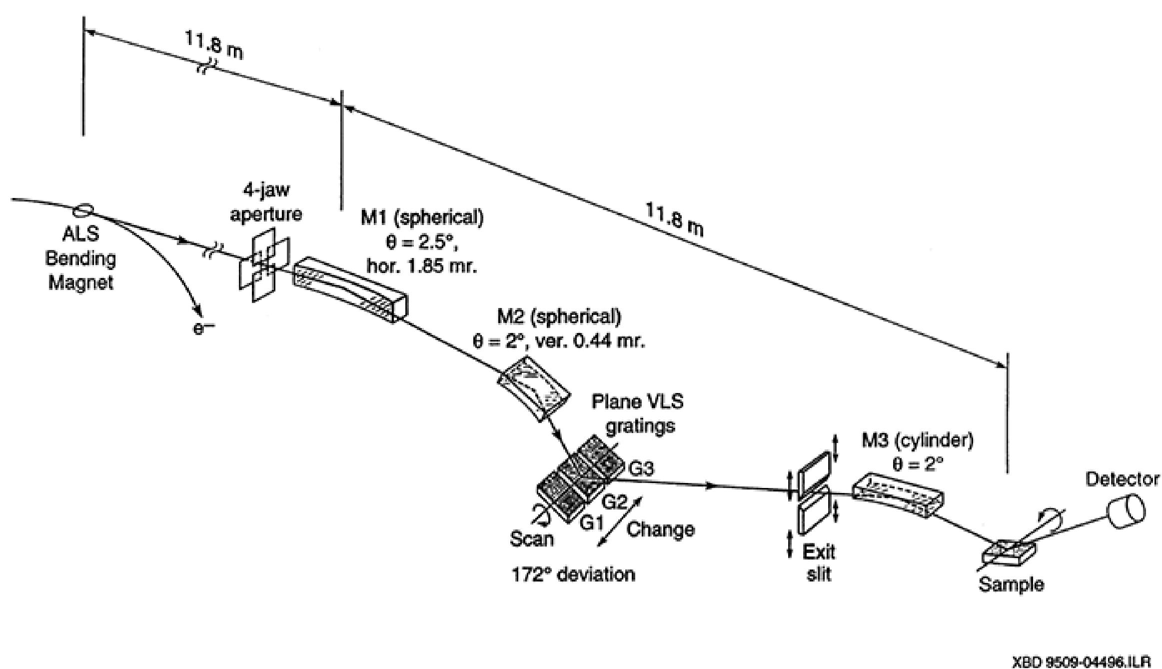

Figure 2.8 Schematic for Beamline 6.3.2 at the Advanced Light Source. This diagram shows how the light is attenuated, reflects off the sample and hits the detector. Schematic courtesy of Underwood et. al. [9].

1. The data were first normalized by dividing by the beam current of each separate data point to compensate for the slight variation in the photon flux due to beam current variation.

2. We subtracted the dark current to remove the background offset. Using the dark current scans we took at the ALS , we found that the dark current was dependent upon angle, particularly at 22 degrees. This can be from some characteristic of the chamber, seen in Fig. 2.3, that would scatter more of the light in that direction or from a way the wires are bent at that location. We fit the dark current scans to a polynomial of order 5 and used this to find the noise in the system. We then took each point of our non-specular reflectance data and subtracted the corresponding dark current to get more clear data.

3. In order to properly interpret our results, we had to calculate the statistical error. We considered the following variances in our data:

   (a) The first is from subtracting our dark current. To compensate for this we used the different dark current scans to determine the variance in the data.

   (b) The uncertainty in the CEM is found using the square root of the number of photons counted by the channeltron. Poisson statistics show that when counting the number of random events, the counted number is distributed in a Poisson distribution. A variance in a Poisson distribution is equal to the square root of the number of counts. This principle applies to the number of photons counted, which is why we used Poisson statistics to find this error.

   (c) The third error is variance from a smooth curve. We fit the data to a smooth spline curve using the code found in Appendix A on page 52. We assumed that the data formed a smooth curve as a function of angle and that large variations in the data were noise. When we saw jumps or bumps in the data as we were taking scans, we would rescan the same area to see if it truly was a feature or if it was noise. In the majority of the

cases, the bumps would go away justifying this assumption.

4. Once we found the different variances, we combined them to form one total error. For the photodiode we used a sum of squares as seen in Eq. 2.1 and formatted error bars on our data.

$$\sigma = \sqrt{(\sigma_{dark})^2 + (\sigma_{spline})^2} \tag{2.1}$$

   For the CEM we used the larger of the Poisson error or the variance from a smooth curve for the error bars.

5. At this point we had to scale the data properly, so we divided all of the values by the gain of the detector. The result of these calculations was to have data sets with error bars and an initial scaling.

6. To combine the individual sets of data into one combined curve, we found the region of each consecutive set of data that overlapped and found the ratio of the signal in the overlapping regions. We started from the runs containing the specular peak and then worked our ways out to the wings on each separate side.

7. Once all of the runs were scaled and combined, the resulting curve showed a complete non-specular reflectance curve. This curve was then normalized to show reflectance per unit angle using the following steps:

   (a) First we had to find the reflectance at a given angle. While at the ALS we also took a series of θ-2θ scans; these were taken without the slit on the detector. These are where we would run a scan and move the sample by one degree and the detector by 2 degrees so we were always measuring the specular peak. We used these scans to calculate the intensity, I of the specular peak for each sample angle.

   (b) Next we found I_0, i.e. the intensity of light going straight into the detector, from other scans taken at each separate wavelength used in our sample analysis.

(c) The reflectance of the sample was then calculated using Eq. 2.2, where D is the dark current, G_I is the gain of the intensity scan and, and G_0 is the gain of the I_0 scan. Since we are dividing I by I_0 and we used the same detector, filter, and order sorter filter, the systematic error associated with each one cancels out. This allows us to not have to consider systematic error here.

$$r = \frac{(I - D) * gain}{I_0 - D) * gain} \tag{2.2}$$

(d) We then took the integral of the combined reflectance curve to find our computed reflectance.

(e) Using the computed reflectance and the theoretical reflectance we were able to find a factor to properly scale our non-specular reflectance curve to find the reflectance per unit angle.

This method assumes that all of the light reflected off the sample hits the detector without a slit. We verified this by integrating the non-specular reflectance curve over the angular acceptance of the detector and compared it to the integral of entire range of the non-specular reflectance curve. We found that the integrated reflection in the detector was 99.82 percent of the total reflection making this assumption valid.

8. The normalized data can be used to find a more complete index of refraction for each of the samples as well as allowing us to estimate the RMS surface roughness.

The complete curve was compared to theoretical reflectance using code for Huygens' method created by Steve Turley. The Huygens' method calculations, discussed in Section 1.5 on page 10, are done by taking a smooth surface and randomly adding noise. We took the Fourier transform of the resulting surface to see how much it varies at each point. We multiplied the transform by a Gaussian curve to remove the higher frequencies and bias the surface towards the lower

frequencies, or a surface with less variance. This creates a more real surface with surface roughness in a reasonable tolerance. We compared this data to the ALS data to find the RMS surface height and the spatial frequency distribution of each sample.

Chapter 3

Results and Analysis

3.1 Introduction

The methods currently used to measure the surface roughness of the thin films are not sufficiently able to determine the RMS surface height and the spatial frequency of the roughness. We hope that our methods, particularly Huygens' method and geometrical optics discussed in this paper, are able to describe the non-specular scattering from surfaces with roughness having spatial frequencies much less than one over the wavelength. Using the analysis described in Chapter 2 Section 2.3, the scans taken at the ALS showed us the reflectance of each sample. We compared the reflectance from various theoretical samples to our data to find the RMS height and spatial frequency roughness of our uranium oxide thin films.

3.2 Huygens' Calculations

Using the Huygens' method discussed in 1.5, on page 10, we were able to create different model surfaces and see how light reflected off each at different angles. The first surface we created was a flat surface with a length of 2000 wavelengths. The reflectance from this flat surface is shown

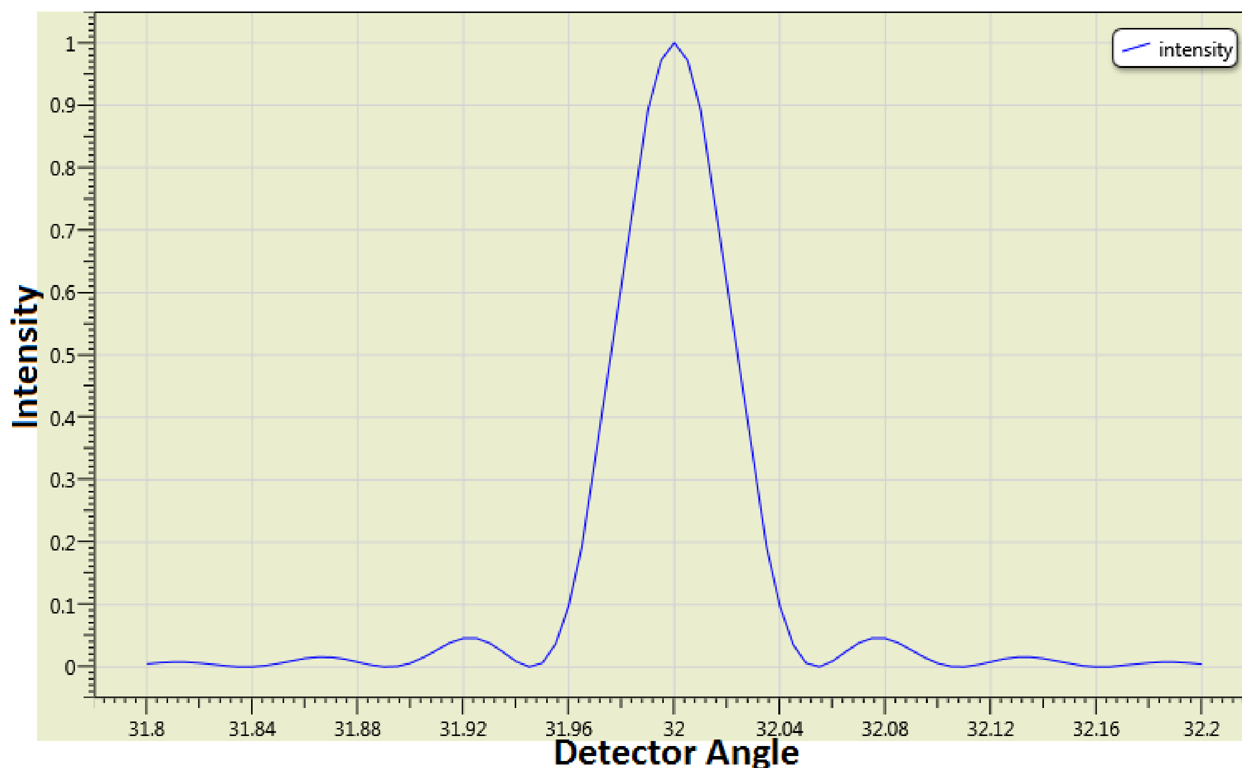

Figure 3.1 Reflection from a flat surface using Huygens calculations. Notice the effects of diffraction causing the non-specular reflectance.

in Fig. 3.1. The effects of diffraction can be seen here, as diffraction broadens the central peak as well as adding side peaks. It is important to note, however, that the spread is very limited and is only 0.2 degrees above and below the specular peak; the angular resolution of beamline 6.3.2 is plus or minus $1/10$ of a degree [9].

If we have a bigger beam, or a beam that interacts with more surface area, then there will be less diffraction. We then used a surface 5 times larger than the previous surface to obtain the reflection seen in Fig. 3.2, which has the same horizontal scale as Fig. 3.1. The beam at the ALS has a spot size of 300 x 100 μm at the surface of the sample [9]. This means the beam is interacting with a portion of the sample which has a length between 10,000 and 120,000 wavelengths, depending on the wavelength used. At these dimensions, diffraction effects are so small that they are negligible when compared to RMS effects.

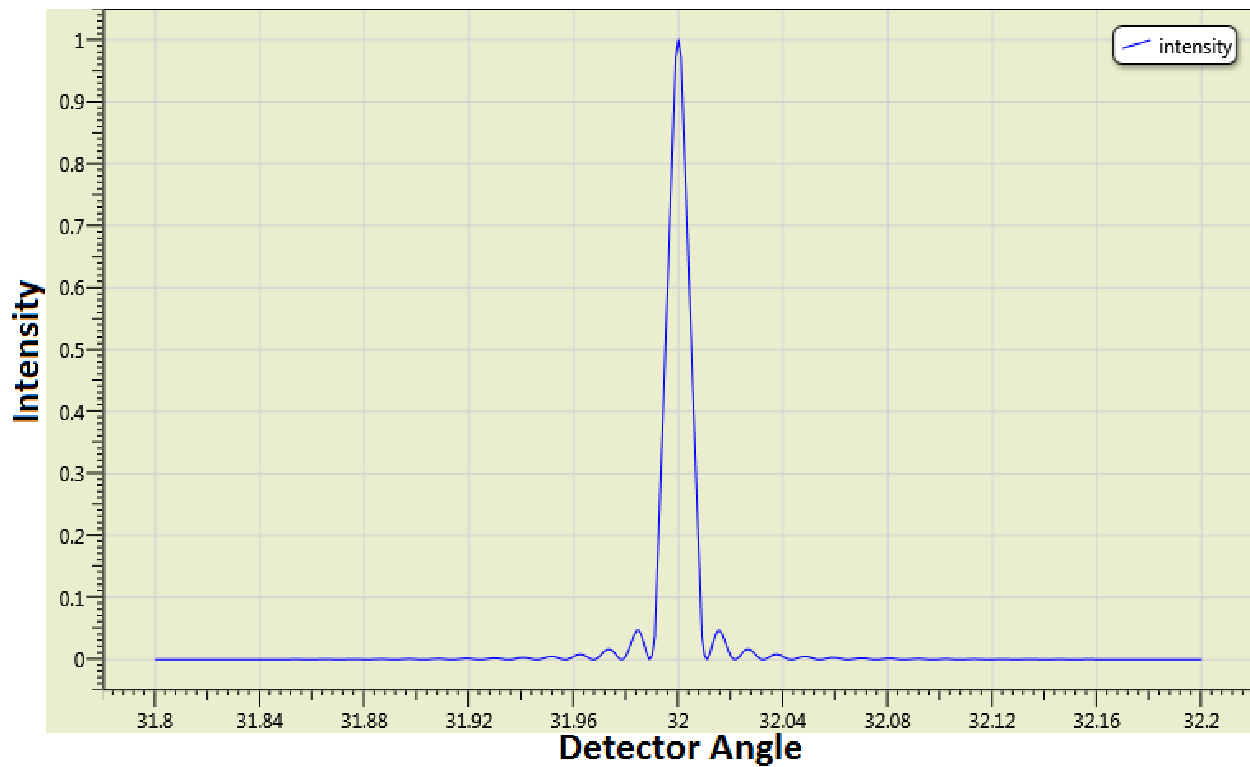

Figure 3.2 Reflection from a long flat surface using Huygens calculations. Notice the effects of diffraction causing the non-specular reflectance are dramatically reduced from those in Fig. 3.1 due to the increased sample size.

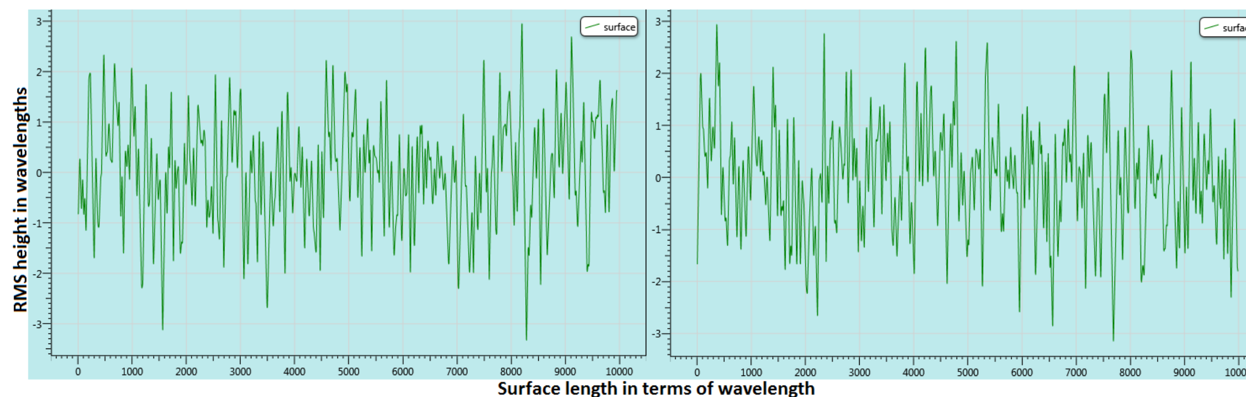

Figure 3.3 We created two random samples with the same RMS height and spatial frequency parameters and calculated the reflectance from both, as seen in Fig. 3.4. Note that although both have an RMS height of 1 wavelengths and a spatial frequency cutoff of 0.1 inverse wavelengths, the location of the features on the surface can vary. We then averaged multiple runs to find an average surface for mirrors with this class of RMS height and spatial frequency roughness.

The code for computing reflectance using Huygens' principle generates a random surface each time the code is run. This allows us to create a variety of surfaces with the same characteristics and compute the reflectance for each one. This can be seen in Fig. 3.3 and Fig. 3.4, which show two surfaces, with an RMS height of 1 wavelength and a spatial frequency cutoff of 0.1 inverse wavelengths, and their reflectance. We then took the data from surfaces with the same RMS height and spatial frequency and averaged the reflectance and the surface features. This shows us how a class of mirrors with those parameters reflect, which is much more valuable than finding how one specific point on a sample reflects.

To see how frequency cutoff affects the qualitative features of the surface, we calculated two separate surfaces with differing spatial frequency components. Both surfaces had an RMS height of 0.5 wavelength but they had frequency cutoffs of 0.1 and 0.01 inverse wavelengths. Notice how in Fig. 3.5 the two surfaces are very different and create very different non-specular reflectance as seen in Fig. 3.6. They both have the same RMS height, but the frequency cutoff is different by an order of magnitude. This shows that methods that use only single parameter fits cannot accurately

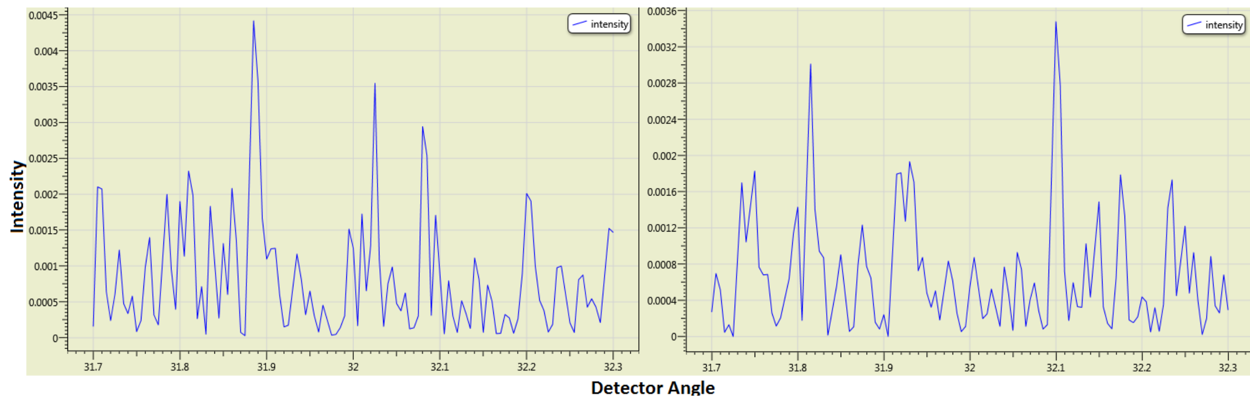

Figure 3.4 We created two random samples with the same RMS height and spatial frequency parameters and calculated the reflectance from both, as seen here. Note that although both have an RMS height of 1 wavelengths and a spatial frequency cutoff of 0.1 inverse wavelengths, the reflection can vary between surfaces. We then averaged multiple runs to find an average reflectance for mirrors with this class of RMS height and spatial frequency roughness.

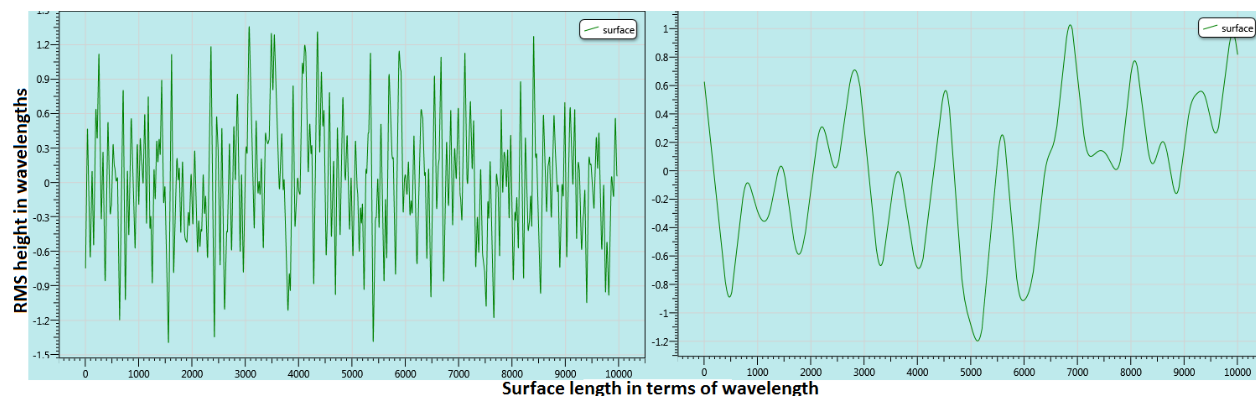

Figure 3.5 We created two random samples with the same RMS height but different spatial frequency parameters and calculated the reflectance from both, as seen in Fig. 3.6. They both have an RMS height of 0.5 wavelength. The left surface has a spatial frequency cutoff of 0.1 inverse wavelengths and the right has a spatial frequency cutoff of 0.01 inverse wavelengths which affects the number of features and their location on the surface.

predict the extent of non-specular scattering.

We also needed to see how RMS height affects the reflection, so we created two surfaces with the same frequency cutoff of 0.001 inverse wavelengths but RMS height of 0.5 and 2 wavelengths.

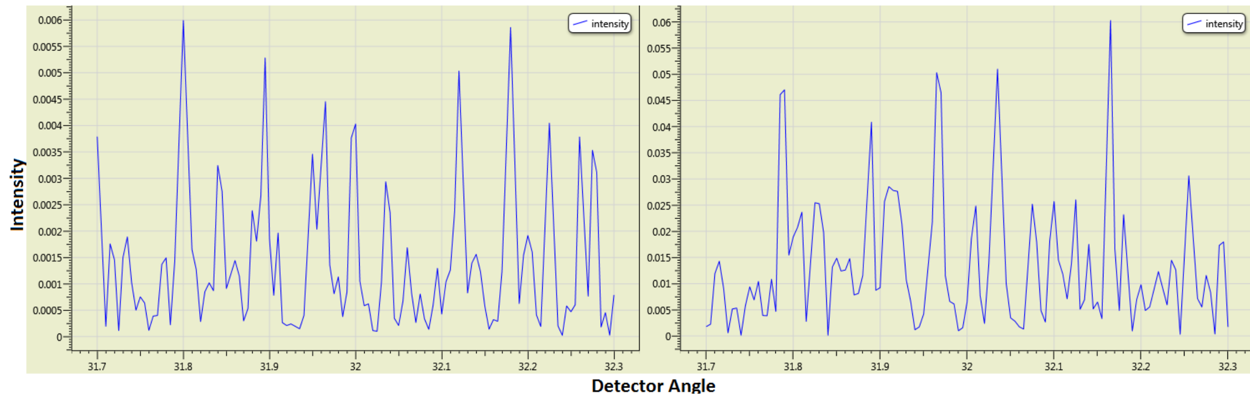

Figure 3.6 We created two random samples with the same RMS height but different spatial frequency parameters and calculated the reflectance from both, as seen here. They both have an RMS height of 0.5 wavelength. The left surface has a spatial frequency cutoff of 0.1 inverse wavelengths and the right has a spatial frequency cutoff of 0.01 inverse wavelengths which affects the amount and angles of scattering. Notice the different orders of magnitude of the intensity along the y-axis.

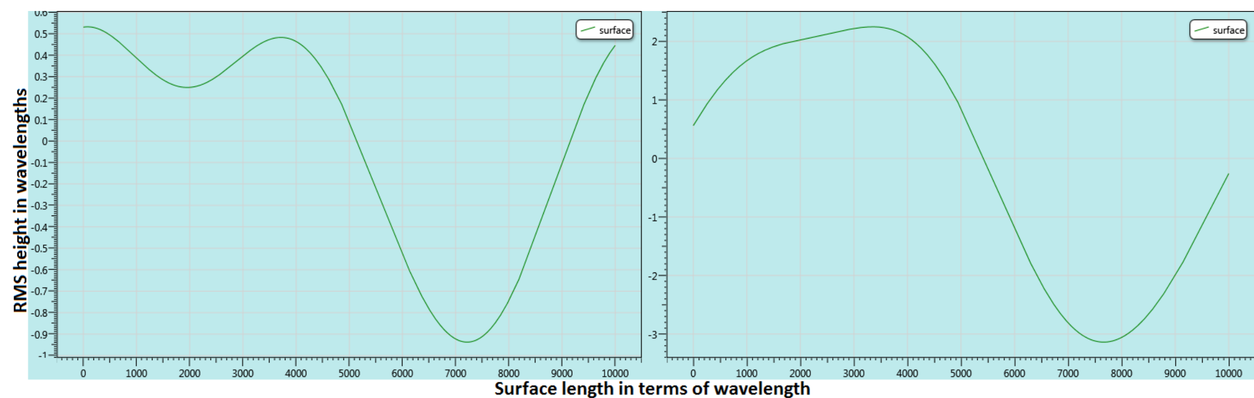

Figure 3.7 We created two random samples with different RMS heights but the same spatial frequency parameters and calculated the reflectance from both, as seen in Fig. 3.8. The surface on the left has an RMS height of 0.5 wavelengths and the one on the right an RMS height of 2 wavelengths, but they both have a spatial frequency cutoff of 0.001 inverse wavelengths. The location of the feature on the surface is similar, but the height is not.

The surfaces can be seen in Fig. 3.7 and their reflectance in Fig. 3.8. The feature on both surfaces look similar in shape, but the heights are very different. This difference shows how much reflectance can change from a surfaces with the same spatial components but differing RMS height.

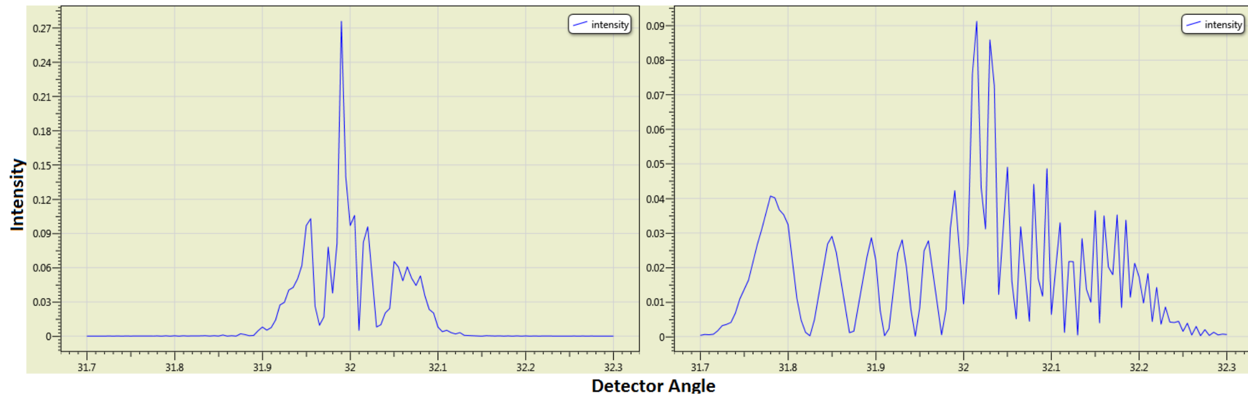

Figure 3.8 We created two random samples with different RMS heights but the same spatial frequency parameters and calculated the reflectance from both, as seen here. The reflection on the left is from a surface with an RMS height of 0.5 wavelengths and the one on the right from a surface with an RMS height of 2 wavelengths, but they both have a spatial frequency cutoff of 0.001 inverse wavelengths. The differing height creates a dramatic difference in reflectance.

3.3 Determining Surface Roughness

By comparing the non-specular reflectance data to the theoretical calculations found using Huygens' principle, we were able to discern more information about our surfaces. As we averaged the reflectance from a variety of surfaces with the same parameters, we noticed that we were not able to fit the non-specular curves as well as we hoped. Our model worked for a simple curve that had a specular peak, but could not match the features in the wings as well as we hoped. This was particularly the case with first non-specular reflectance curve we tried to analyze which had a plateau seen in Fig. 3.9. This figure shows the reflectance per unit angle for uranium oxide sample 1 at 2.5 nm with a fixed incidence angle of 2.5 degrees, on a log scale. Looking at the reflectance we determined that there must be bumps on the surface of the thin film, and the shape of the reflectance meant the bump was roughly quadratic. In order to find a surface that matches this reflectance, we used geometrical optics. This method allows us to determine surface features much larger than a wavelength reasonably well.

To use geometrical optics, we found what percent of the reflected light was represented by the

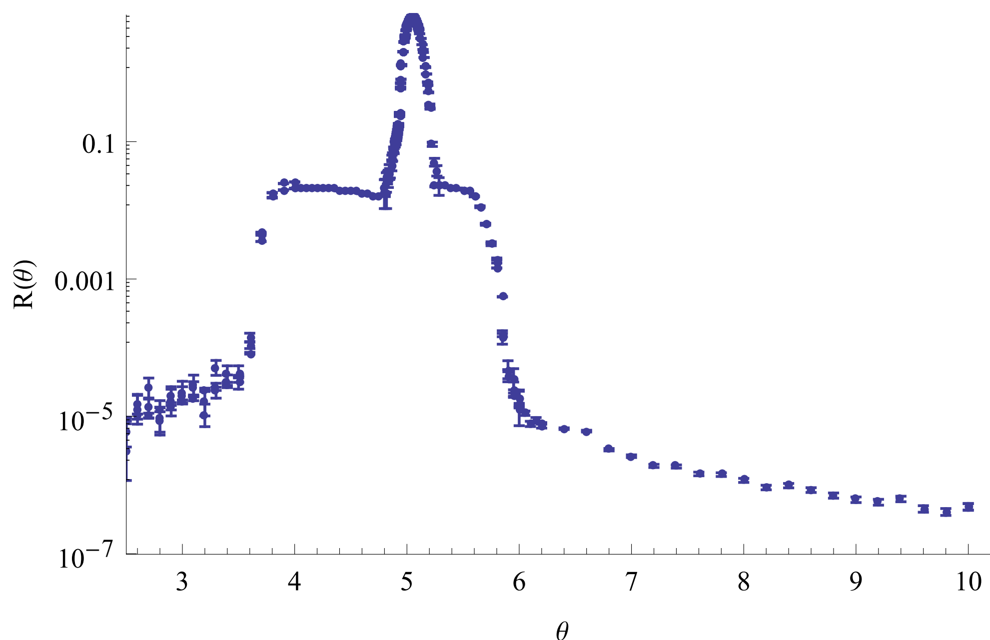

Figure 3.9 Reflection per unit angle for uranium oxide sample 1 at 2.5 nm with a fixed incidence angle of 2.5 degrees, on a log scale. A plateau in the non-specular reflectance is the feature of interest. The curve includes error bars showing statistical error.

peak and what percent was represented in the plateau. First, we found the size of the beam at the surface. The spot size is 300 x 100 μm at the surface of the sample, but this varies upon the angle of the sample [9]. The major axis of the ellipse is perpendicular to the direction the angles were measured, meaning it is constant independent of the sample tilt. We found the modified size of the beam for the sample angle, and found the total area of the beam spot. Using the percent of the reflected light contributing to the plateau and the beam area, we were able to find the area of the bump scattering the light. We were able to create a model surface with this feature and find a histogram of the rays from the surface. Upon computing this, we found that the histogram showed a tall specular peak with a plateau around it, confirming our hypothesis. This histogram can be seen in Fig. 3.10.

Once we had a correct model, we had to find the shape of the feature that would cause the right peak to plateau ratio. We found that a bump 91.2 microns in diameter and 0.25 microns high is

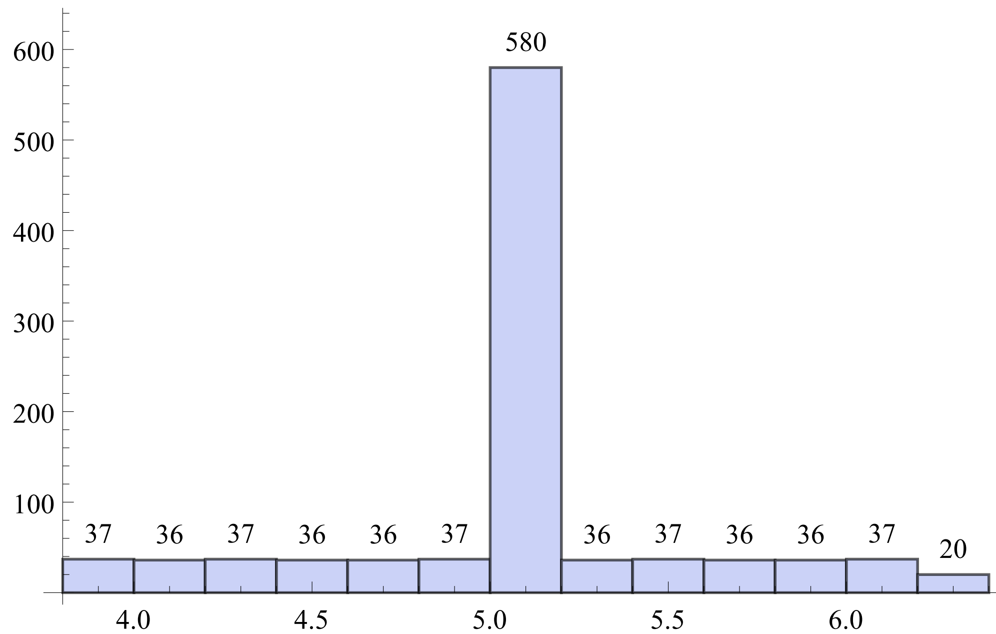

Figure 3.10 Histogram of reflected rays showing a specular peak and a plateau on both sides of the peak.

responsible for the non-specular reflection. The surface with this feature can be seen in Fig. 3.11 and the computed reflectance from this surface in Fig. 3.12. It is important to note that Fig. 3.9 is on a log scale, while Fig. 3.12 is on a linear scale. However, they both have the same peak to plateau ratio and the specular peak has the same approximate width.

A bump this size can be seen using an SEM, so we were able to look at our sample to check our calculations. A picture taken by the SEM can be seen in Fig. 3.13. It is immediately obvious that there is no bump 91.2 microns wide on this surface. Therefore, the reflectance from each one of the small bumps seen in the SEM scan add constructively to create the reflection as if it was from one bump 91.2 microns in diameter.

There were more non-specular reflectance curves showing plateaus; however, no other scans taken on sample 1 showed similar reflectance. One possible explanation is that the 100 μm ellipse of the beam is more spread out at shallow grazing angles, causing a larger beam size. This beam picks up more bumps which then have a more substantial effect on the reflectance. Also, our beam

Figure 3.11 Model of the surface of uranium oxide sample 1 showing the feature causing the non-specular reflectance. Units on both axis are in terms of microns.

Figure 3.12 Histogram of the rays reflecting from uranium oxide sample 1 using the surface seen in Fig. 3.11. This has the same peak to plateau ration as Fig. 3.9. Detector angle is along the x-axis and the y-axis is proportional to intensity.

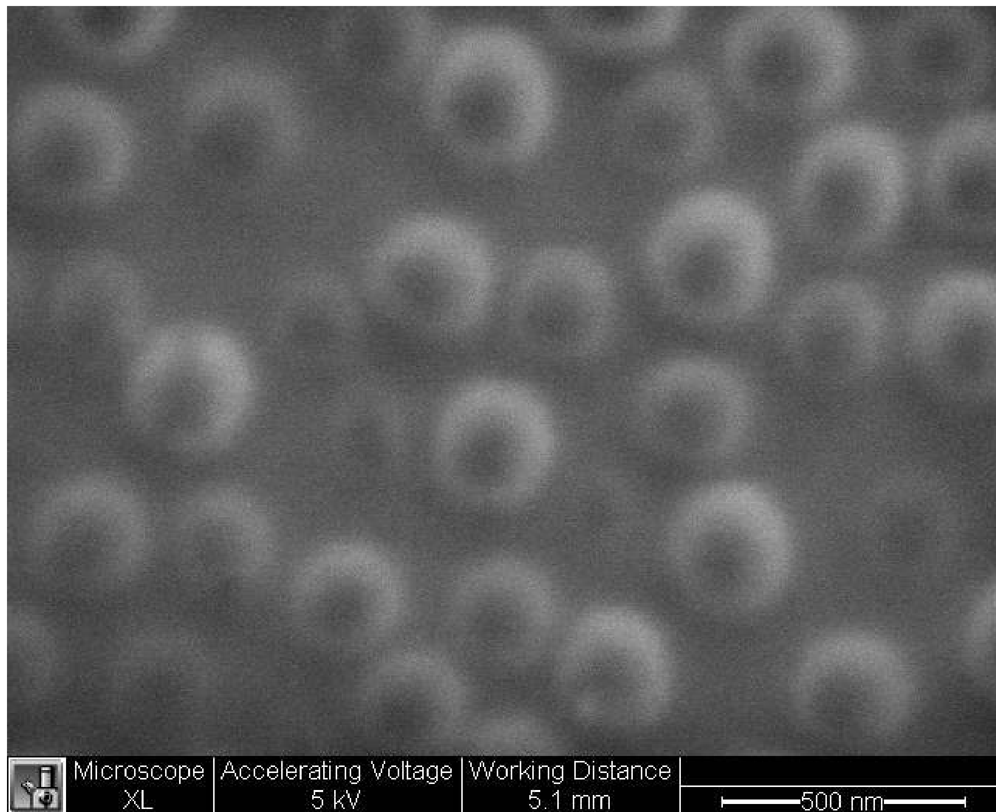

Figure 3.13 Scan taken by an SEM of uranium oxide sample 1 showing the features responsible for the non-specular reflection.

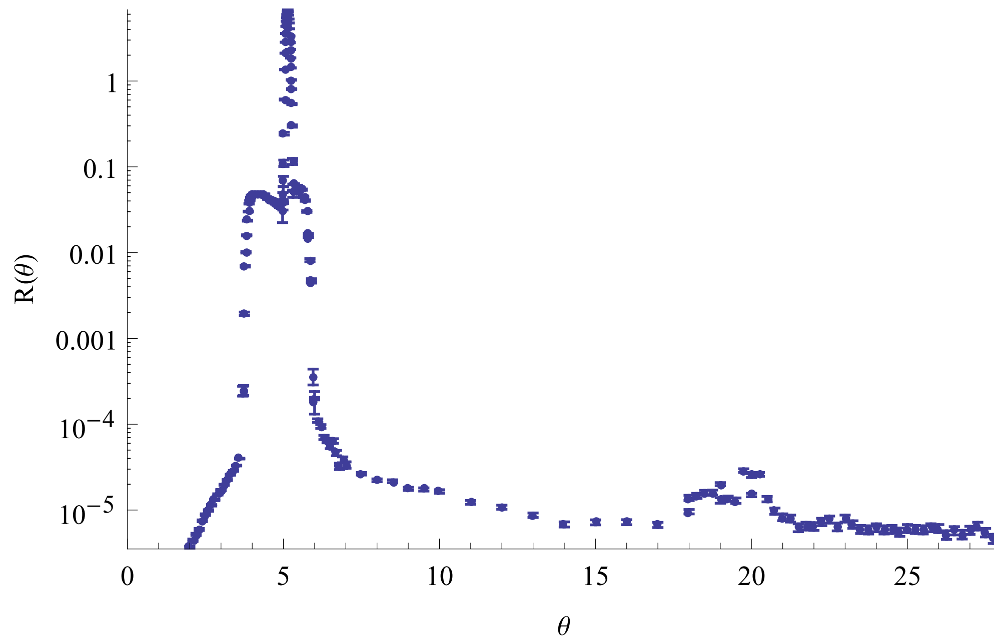

Figure 3.14 Reflection per unit angle for uranium oxide sample 2 at 2.5 nm with a fixed incidence angle of 2.5 degrees, on a log scale. A plateau in the non-specular reflectance is the feature of interest. The curve includes error bars showing statistical error.

is only illuminating one side of the bump, rather than the whole bump. This causes the scattering to be more pronounced and causes the plateau to be larger on one side of the peak than the other; a perfectly illuminated bump would cause a plateau that is equal on both sides of the peak.

When calculating the reflectance per unit angle for uranium oxide sample 2 at 2.5 nm with a fixed incidence angle of 2.5 degrees, we saw another plateau which can be seen in Fig. 3.14. Using the same method outlined above, and finding the same peak to plateau ration seen in the curve of reflectance per unit angle, we calculated that a feature 175.215 microns in diameter and 0.5601 microns high is responsible for the non-specular reflection. This surface and its reflection can be seen in Fig. 3.15 and Fig. 3.16 respectively.

We found one more plateau on the reflectance per unit angle graph for uranium oxide sample 3 at 15 nm with a fixed incidence angle of 10 degrees, see Fig. 3.17. This is interesting, because we did not see this same plateau at the lower incident angles for this sample, and we are unsure why.

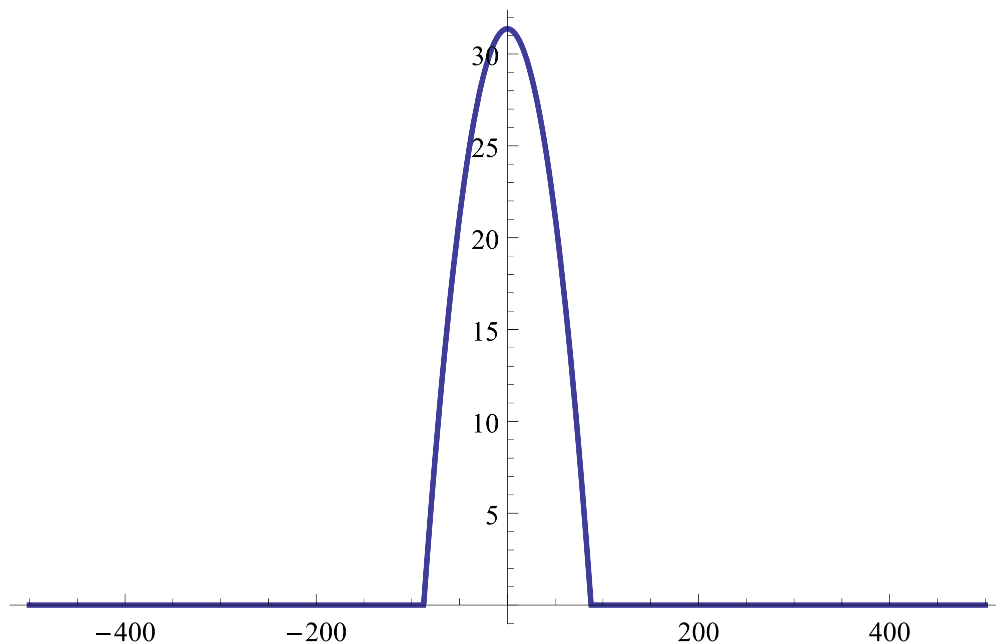

Figure 3.15 Model of the surface of uranium oxide sample 2 showing the feature causing the non-specular reflectance. Units on both axis are in terms of microns.

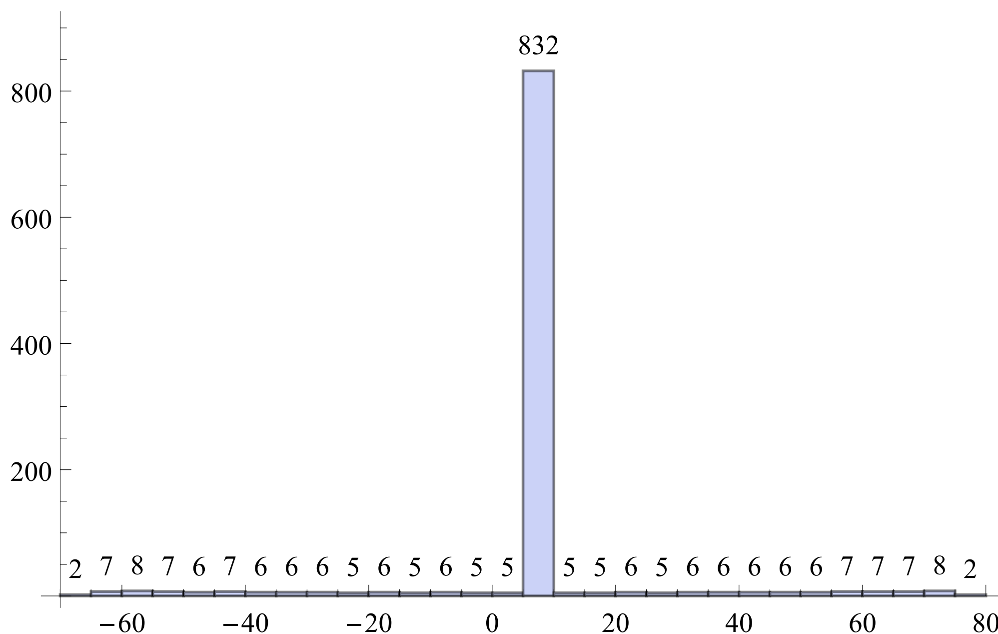

Figure 3.16 Histogram of the rays reflecting from uranium oxide sample 2 using the surface seen in Fig. 3.15. This has the same peak to plateau ration as Fig. 3.14. Detector angle is along the x-axis and the y-axis is proportional to intensity.

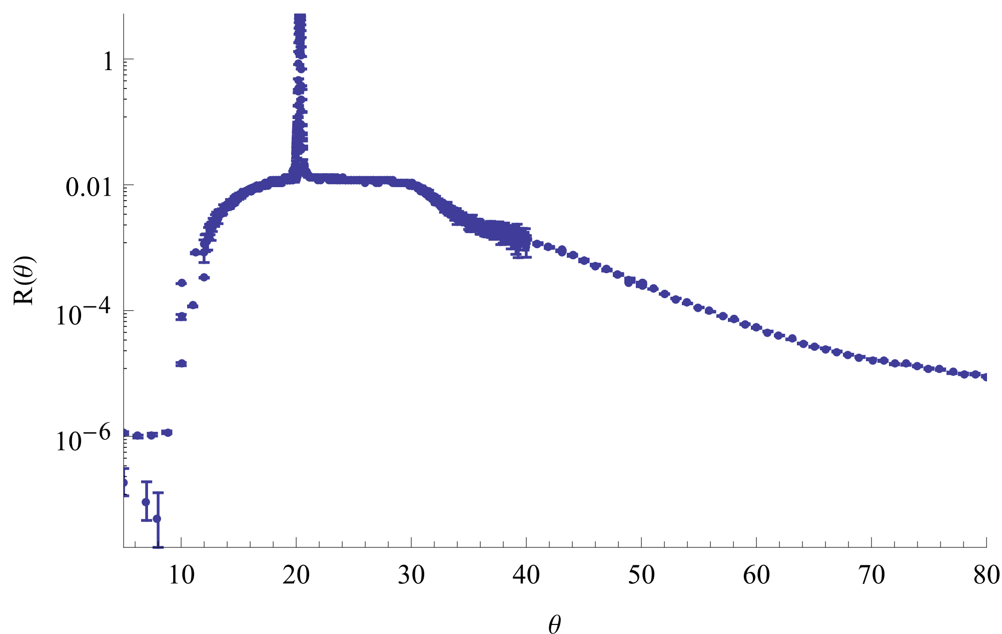

Figure 3.17 Reflection per unit angle for uranium oxide sample 3 at 15 nm with a fixed incidence angle of 10 degrees, on a log scale. This plateau is particularly interesting because it is not seen in the non-specular reflectance scans at lower incident angles for this sample. The curve includes error bars showing statistical error.

Using the data with the plateau, however, we did calculate that to cause the scattering seen here must be caused by a feature 121.52 microns wide and 2.3271 microns high. This surface and the corresponding reflection can be seen in Fig. 3.18 and Fig. 3.19 respectively.

We then moved to the data we could match using the Huygens' calculations. While working through the analysis we found that our surface model was incapable of computing a reflectance that matched our experimental data. We found that we were able to match some of the specular peaks to a surface with one frequency cutoff, but the wings and other features seen required a higher frequency cutoff. This means that a Gaussian cutoff is the wrong shape to use to be able to model the entire surface. In order to account for this, we found an RMS height that was able to fit both the peak and the wings. We then created two different model surfaces with the same RMS height, but different spatial frequencies; a higher frequency cutoff was used to model the surface contributing to the reflection seen in the wings and a lower frequency cutoff to find a surface causing the proper

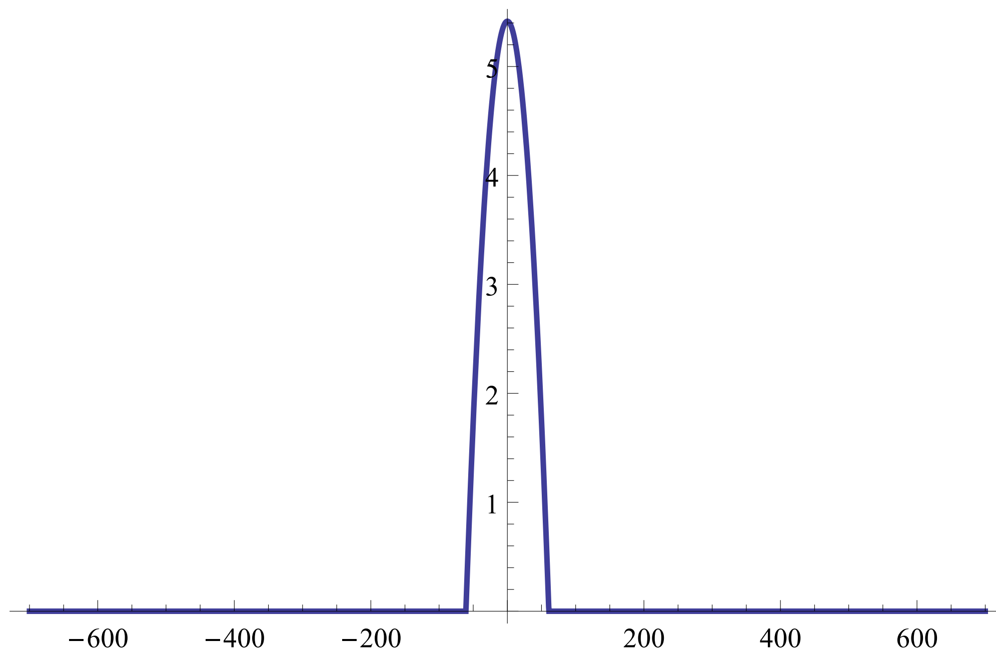

Figure 3.18 Model of the surface of uranium oxide sample 3 showing the feature causing the non-specular reflectance. Units on both axis are in terms of microns.

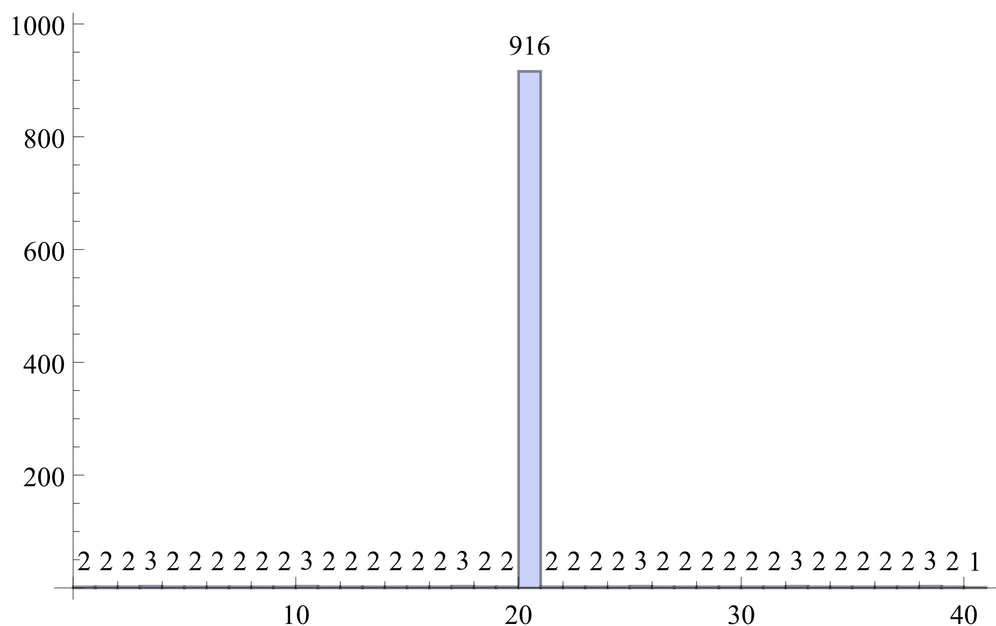

Figure 3.19 Histogram of the rays reflecting from uranium oxide sample 3 using the surface seen in Fig. 3.18. This has the same peak to plateau ration as Fig. 3.17. Detector angle is along the x-axis and the y-axis is proportional to intensity.

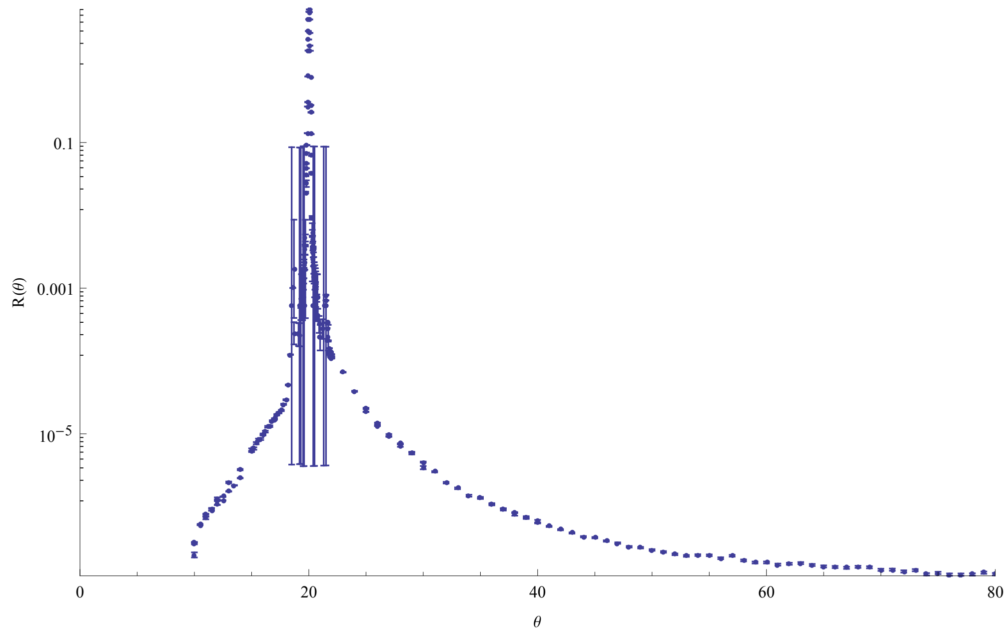

Figure 3.20 Reflection per unit angle for uranium oxide sample 1 at 15 nm with a fixed incidence angle of 10 degrees, on a log scale. The curve includes error bars showing statistical error which show the variance at two smaller peaks on both sides of the specular peak. Fig. **??** shows these features without the error bars.

specular peak. This means our surface varies more than our model can account for making exact classification of the RMS height and spatial frequency roughness impossible.

While we were not able to find any perfect fits, we were able to find some theoretical reflectance curves that we can use to begin interpreting our data. The best fit was found for uranium oxide sample 1 at 15 nm with a 10 degree incident angle; the reflectance per unit angle curve can be seen in Fig. 3.20. To the right and the left of the specular peak there are two smaller peaks. These peaks occur where different data sets were combined to show the total curve, so it is unsure if they are true features or are constructs of the data taking process. There are large error bars shown at both sides of the peak, see Fig. 3.20, which come from this variance in the data. The data without error bars can be seen in 3.21 showing these two smaller peaks. Using Huygens' method we were able to create a surface that models this reflectance using an RMS height of 2 wavelengths and a frequency cutoff of 0.001 inverse wavelengths. We averaged 10 different reflectance curves

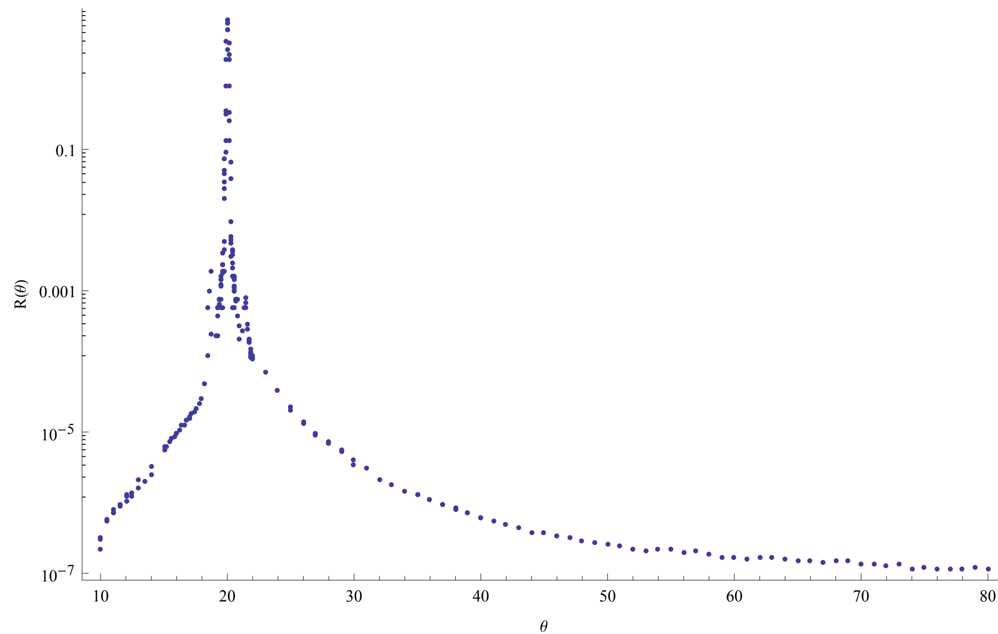

Figure 3.21 Reflection per unit angle for uranium oxide sample 1 at 15 nm with a fixed incidence angle of 10 degrees, on a log scale. The error bars are removed from Fig. 3.20 to show the non-specular peaks on both sides of the specular peak.

from samples with these same parameters to obtain the reflection seen in Fig. 3.22. The surface used to find this reflection can be seen in Fig.3.23. It is useful to visually compare this computed reflectance to reflectance per unit angle on a linear scale, which can be seen in Fig. 3.24. The specular peak found using our data from ALS has a FWHM of 0.5 degrees and the FWHM of the specular peak found using Huygens' method has a FWHM of approximately 0.5 degrees as well.

After finding the specular peak, we fit the wings to a computed surface as well. This time we did not look for a specular peak; instead, we wanted to match the nons-specular reflectance. In order to match the non-specular portion of the graph, we varied the frequency cutoff parameter. The spatial frequency of the features on the surface of a thin film can vary with location, but the RMS height is the same across the whole sample. We found that a surface with an RMS height of 2 wavelengths and a frequency cutoff of 0.04 inverse wavelengths gives the reflectance seen in Fig. 3.25; the surface can be seen in Fig. 3.26. This data has a slope of $4x10^{-4}$. The slope near the

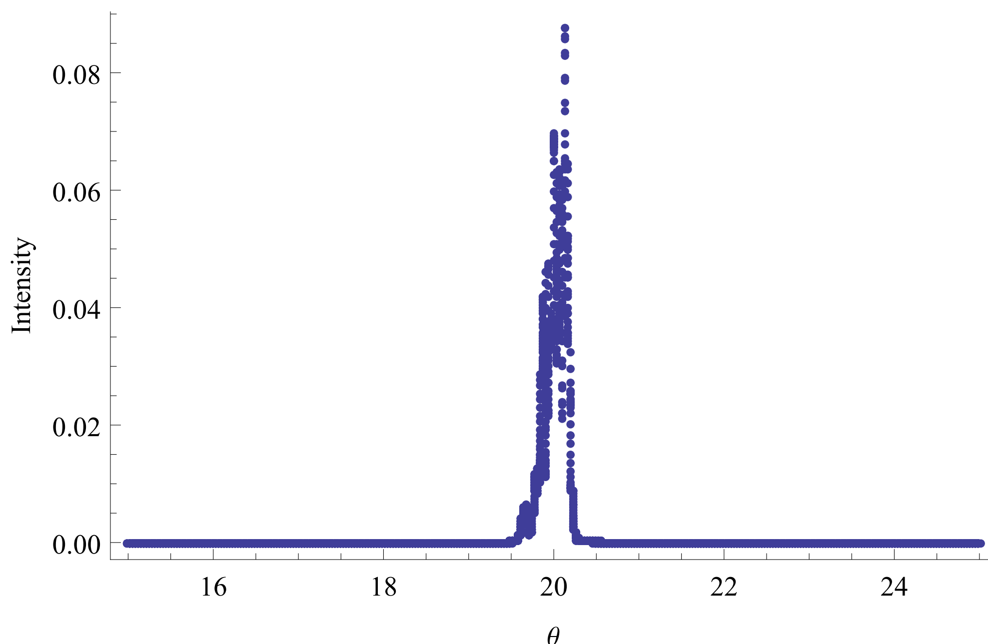

Figure 3.22 Computed reflection using Huygens' method for uranium oxide sample 1 at 15 nm with a fixed incidence angle of 10 degrees.

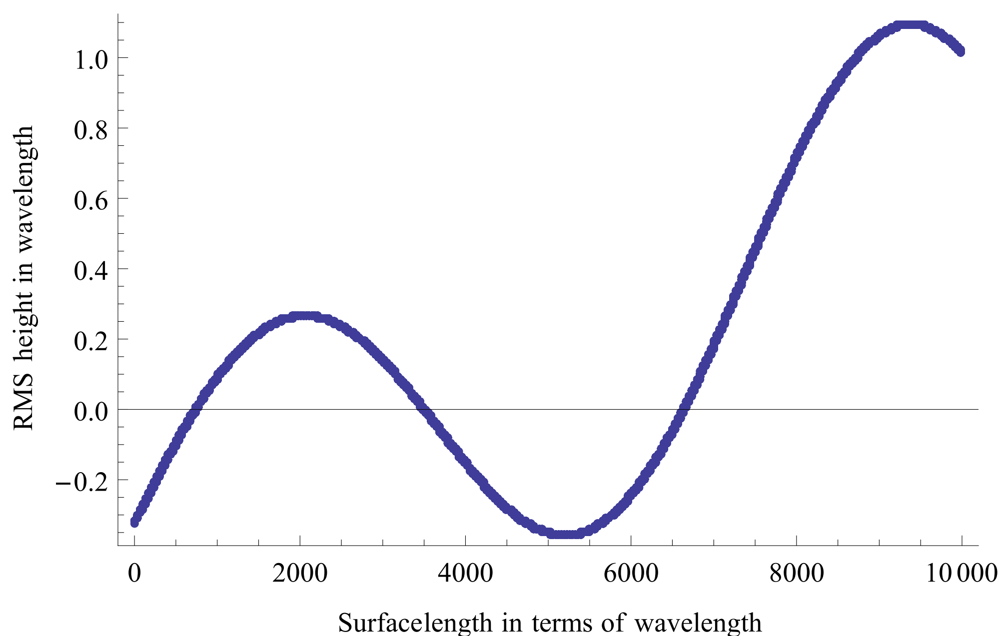

Figure 3.23 Theoretical surface found using Huygens' program. The surface has an RMS height of 2 wavelengths and a frequency cutoff of 0.001 inverse wavelengths. This surface was used to compute the reflectance seen in Fig. 3.22.

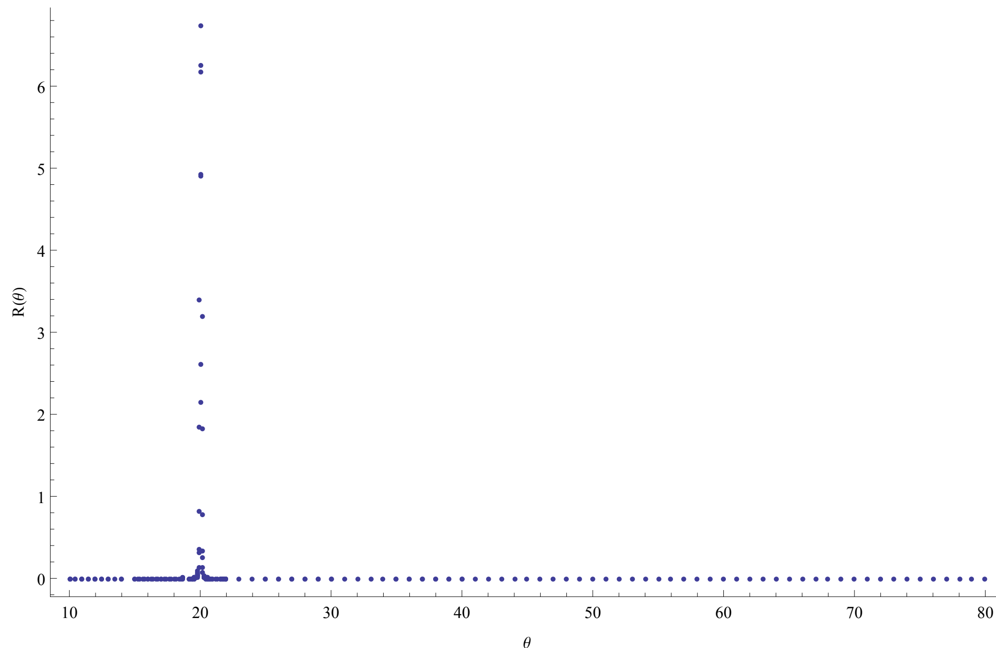

Figure 3.24 Reflection per unit angle for uranium oxide sample 1 at 15 nm with a fixed incidence angle of 10 degrees, shown on a linear scale.

specular peak of Fig. 3.20 is $2x10^{-4}$. The two slopes are comparable, giving validity to our match.

Since this data was taken at 15 nm, an RMS height of 2 wavelengths corresponds to an RMS surface roughness of 30 nm. This is very different than what was found using geometrical optics. We found that at there should be a feature on the surface 0.25 microns high which is a whole order of magnitude larger than the RMS height found using Huygens' method. We also had to use two different spatial frequencies to math the different parts of our data. We do not know for sure what the RMS height of sample 1 is due to the large disagreements between our calculations, but we can use this data to create better surface models in the future to avoid these discrepancies.

We were also able to use Huygens' method to analyze the data taken on sample 2 at 15 nm. The reflectance per unit angle for sample 2 at 15 nm with the sample held at 10 degrees can be seen in Fig. 3.27. We averaged 20 surfaces with an RMS height of 0.25 wavelengths and a frequency cutoff of 0.001 inverse wavelengths, a sample surface with these parameters can be seen in Fig.

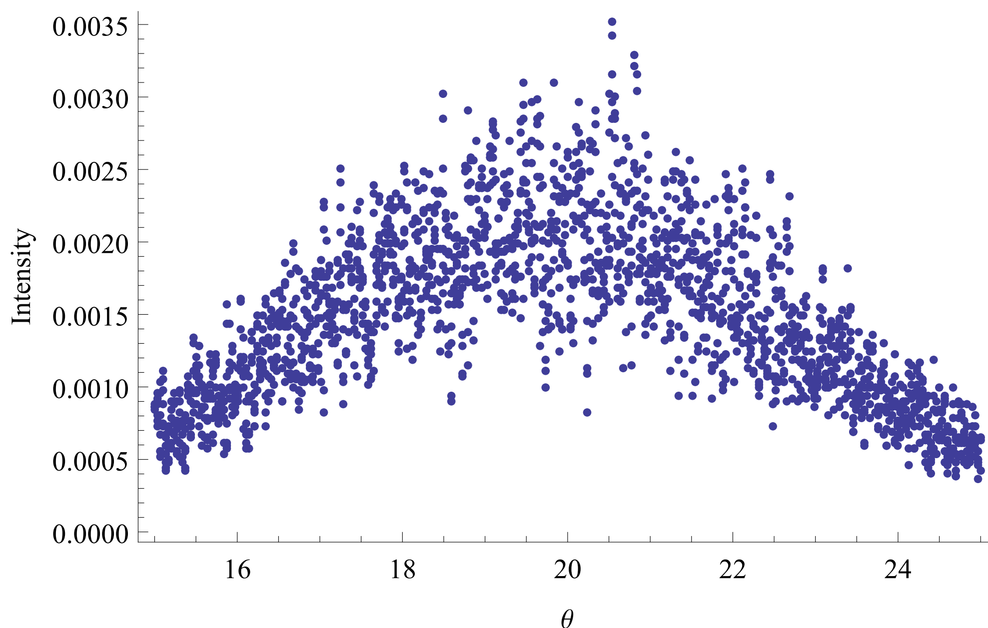

Figure 3.25 Computed reflection using Huygens' method for the non-specular portion of uranium oxide sample 1 at 15 nm with a fixed incidence angle of 10 degrees.

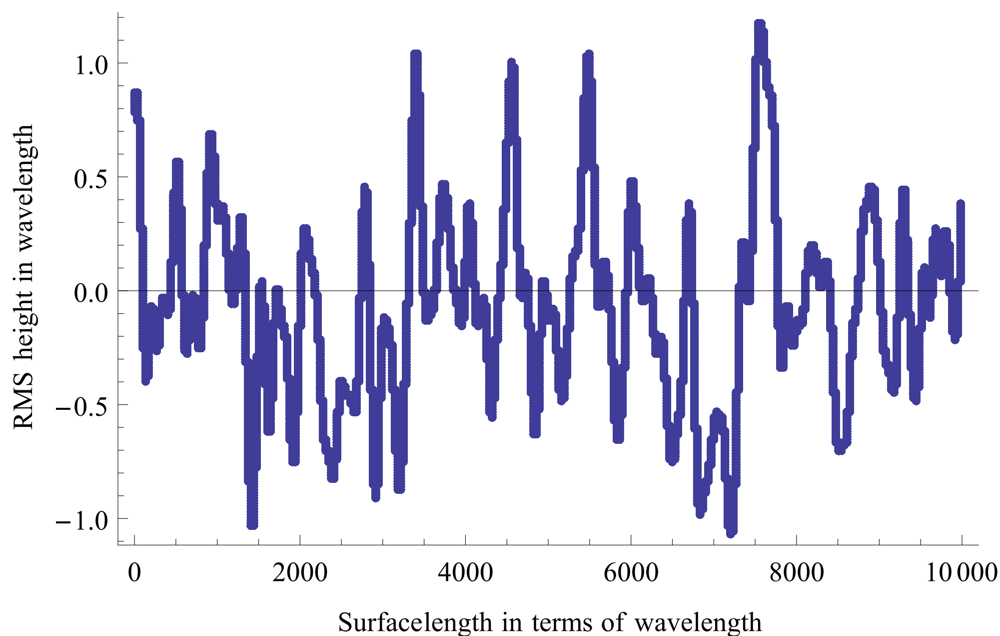

Figure 3.26 Theoretical surface found using Huygens' program. The surface has an RMS height of 2 wavelengths and a frequency cutoff of 0.04 inverse wavelengths. This surface was used to compute the reflectance seen in Fig. 3.25.

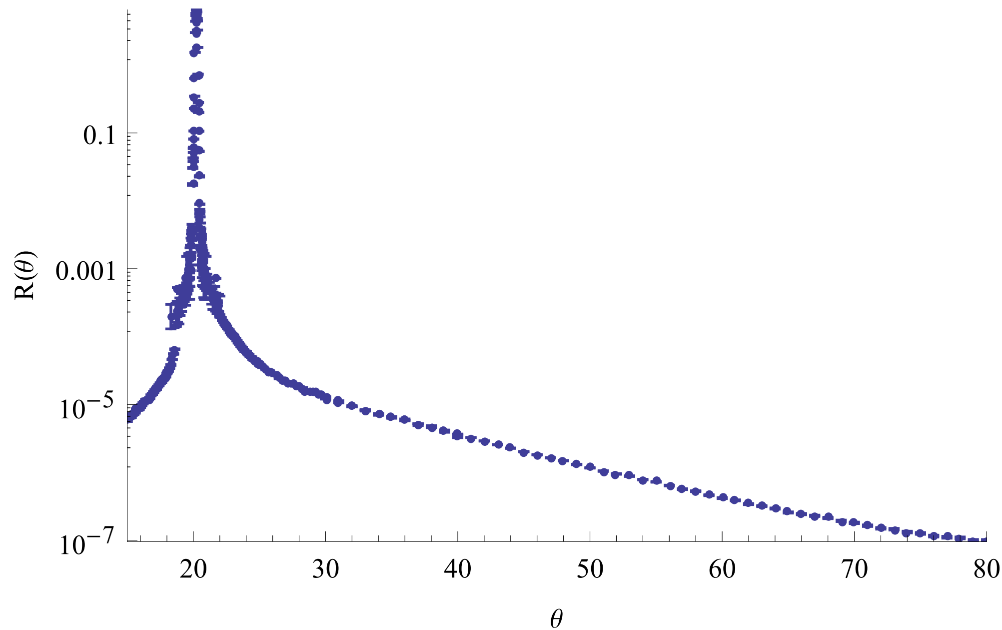

Figure 3.27 Reflection per unit angle for uranium oxide sample 2 at 15 nm with a fixed incidence angle of 10 degrees, on a log scale. The curve includes error bars showing statistical error.

3.28, to produce the reflectance seen in Fig. 3.29. The FWHM of the reflectance found using Huygens' method is 0.1 degrees, while the FWHM of our data is 0.25 degrees. While this is not as good of a match as we hoped, the reflectance found using Huygens' method does show the same features at the bottom of the specular peak. The reflectance per unit angle is shown on a linear scale in Fig. 3.30 for reference.

Using Huygens' method we found the RMS height to be 0.25 wavelengths or 3.75 nm. Using geometrical optics we found that the features must be 0.5601 microns high. This time we have a discrepancy of two orders of magnitude between the two methods. While we are able to match the reflectance per unit angle to theoretical reflectance, we cannot determine the surface roughness of our samples.

While we calculate reflectance per unit angle for the three samples at other wavelengths, we were not able to accurately model any more data. Our models are not able to compensate for the

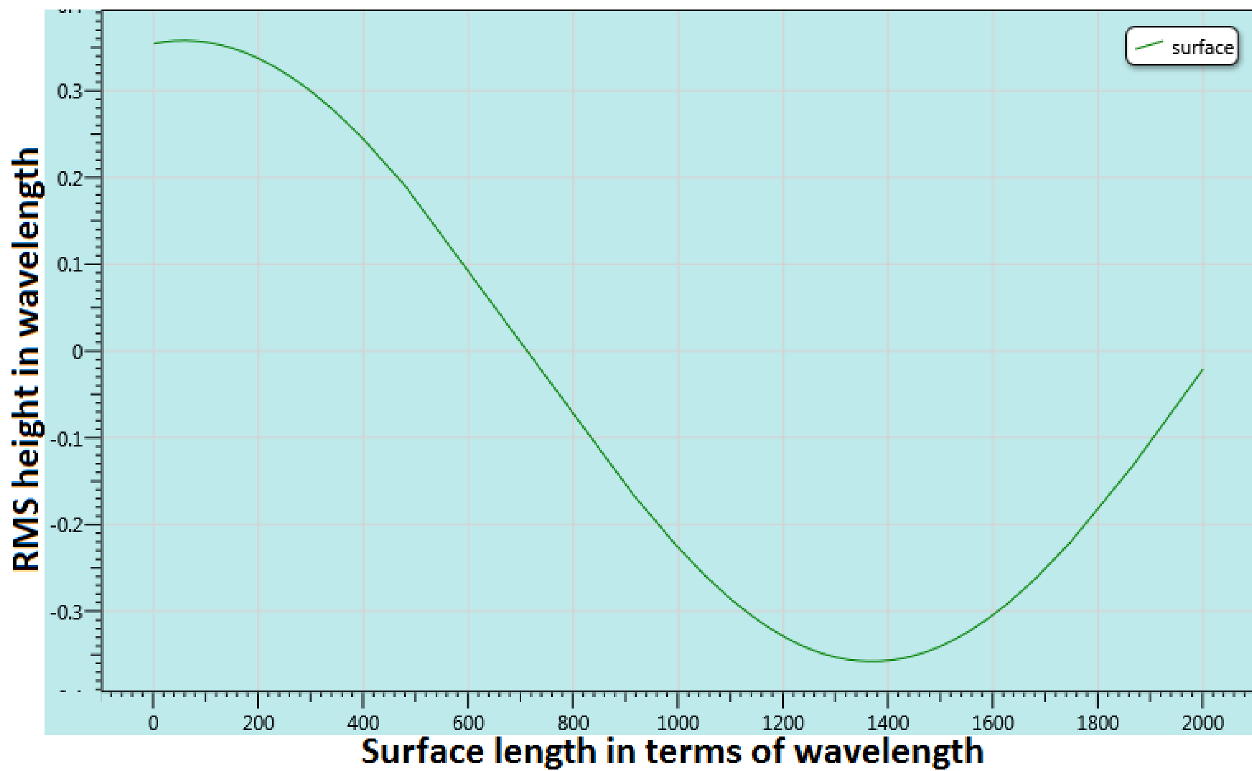

Figure 3.28 Theoretical surface found using Huygens' program. The surface has an RMS height of 2 wavelengths and a frequency cutoff of 0.04 inverse wavelengths. This surface was used to compute the reflectance seen in Fig. 3.29.

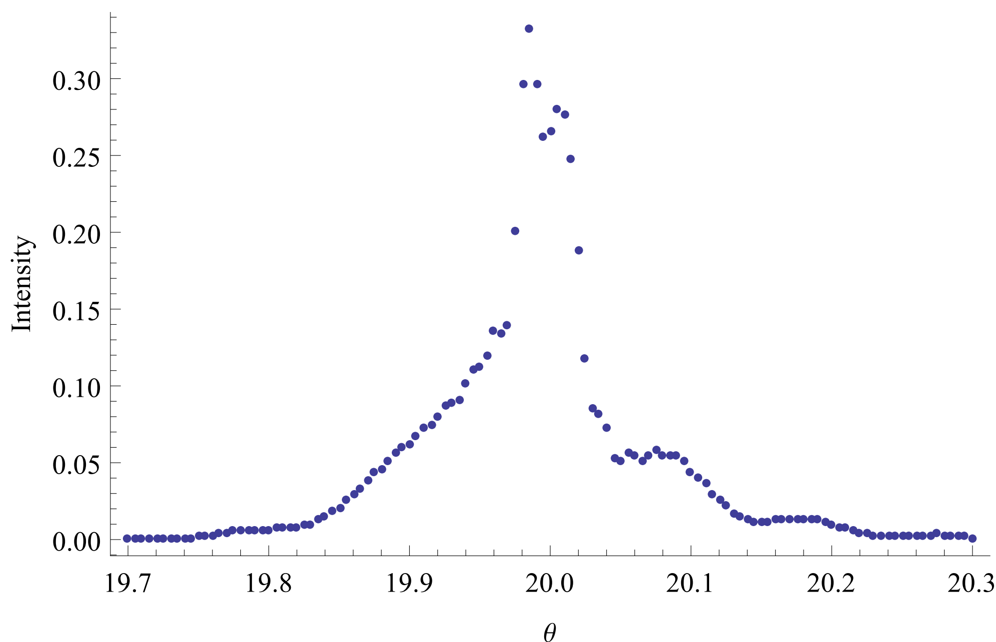

Figure 3.29 Computed reflection using Huygens' method for uranium oxide sample 2 at 15 nm with a fixed incidence angle of 10 degrees.

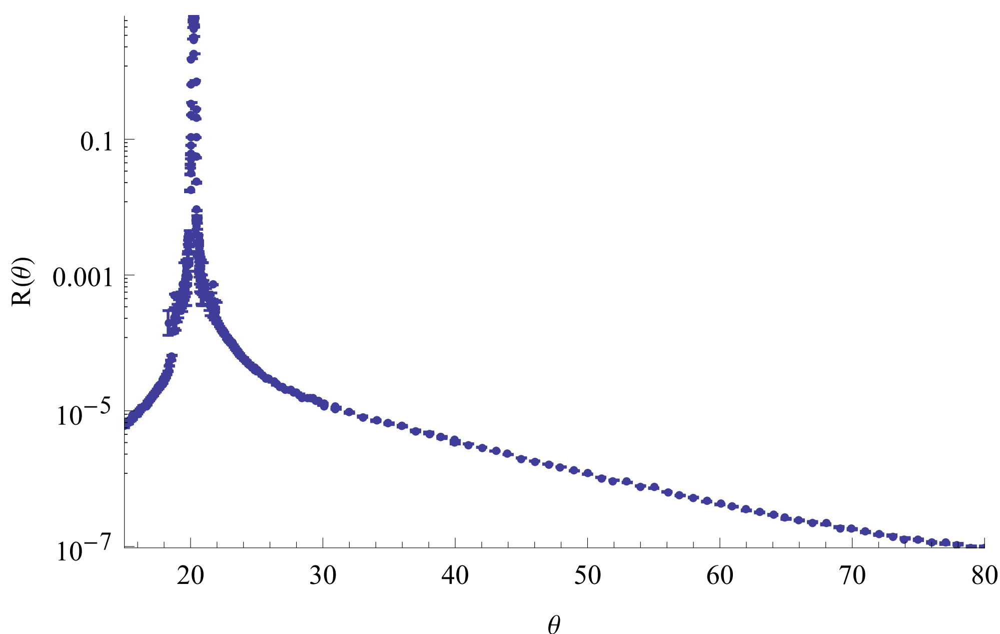

Figure 3.30 Reflection per unit angle for uranium oxide sample 2 at 15 nm with a fixed incidence angle of 10 degrees, on a linear scale. The curve includes error bars showing statistical error. Can be used for comparison with Fig. 3.29 which is also on a linear scale.

surface variations sufficiently or able to match up with the features we see in the non-specular reflectance; also, we were not able to get the specular peaks to have the same FWHM. The rest of the reflectance per unit angle curves are in Appendix B on page 53.

3.4 Future Work

Our results were enlightening, but not entirely in the way that we were hoping. We were unable to quantify our surfaces due to the surface variance being higher than we expected. However, we were able to find out more about surfaces than we knew before, but only rudimentary knowledge. To obtain better quantifications of the surface roughness we need a better surface model than the one we are currently employing. The inability to match the wings represents a deficiency in our surface model, so we need to modify it to match this. In order to improve the model we will need to find a way to combine different cutoffs to obtain the correct amounts of high and low frequency spatial frequencies to properly describe our thin films. We will also have to use a better model than the geometrical optics and Huygens' method used for these calculations. This can be done by finding the exact surface current using boundary element methods. This work will be done in the future, building upon what our research group has already done. We hope to be able to create a model accurate enough to describe the non-specular scattering from surfaces with roughness having spatial frequencies much less than one over the wavelength.

Appendix A

Mathematica Code

Mathematica code for a cubic spline function which creates an interpolation that is a smooth function rather than connecting every point:

```
cubicSplSmooth[data_, lambda_] := Module[{M, Knots, X, Dsq, a},
   M = Length@data;
   Knots = Flatten@{1, 1, 1, Range@M, M, M, M};
   X = Table[
     Evaluate@N@BSplineBasis[{3, Knots}, n, t], {t, 1, M}, {n, 0,
      M + 1}];
   Dsq = Differences[X, 2];
   a = LinearSolve[Transpose[X].X + lambda*Transpose[Dsq].Dsq,
     Transpose[X].data, Method -> "Multifrontal"];
   Return[X.a]];
   \label{spline}
```

Appendix B

Graphs

Below are the various graphs of reflectance per unit angle that we were not able to accurately model.

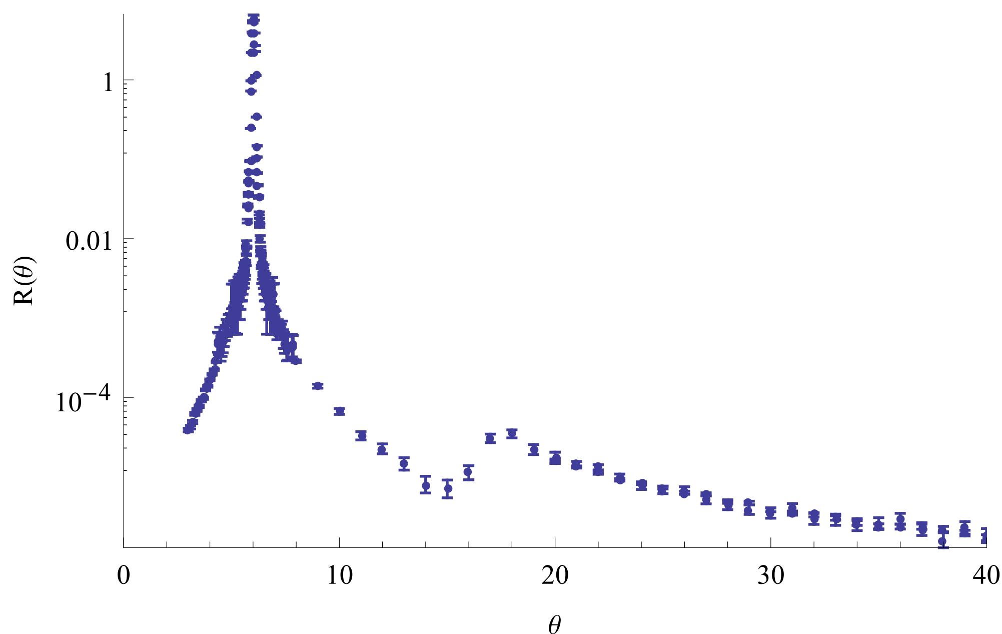

Figure B.1 Reflection per unit angle for uranium oxide sample 1 at 5 nm with a fixed incidence angle of 3 degrees, on a log scale. The curve includes error bars showing statistical error. We were unable to fit the FWHM of the specular peak to any reflectance using Huygens' method.

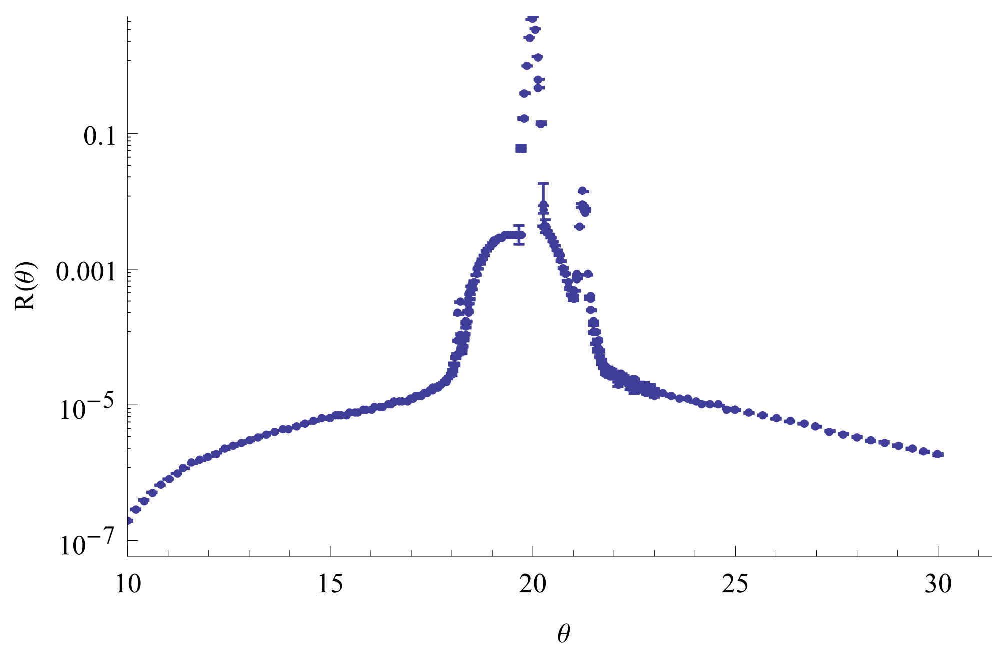

Figure B.2 Reflection per unit angle for uranium oxide sample 1 at 30.4 nm with a fixed incidence angle of 10 degrees, on a log scale. The curve includes error bars showing statistical error. Our current surface models cannot model the features seen in this curve.

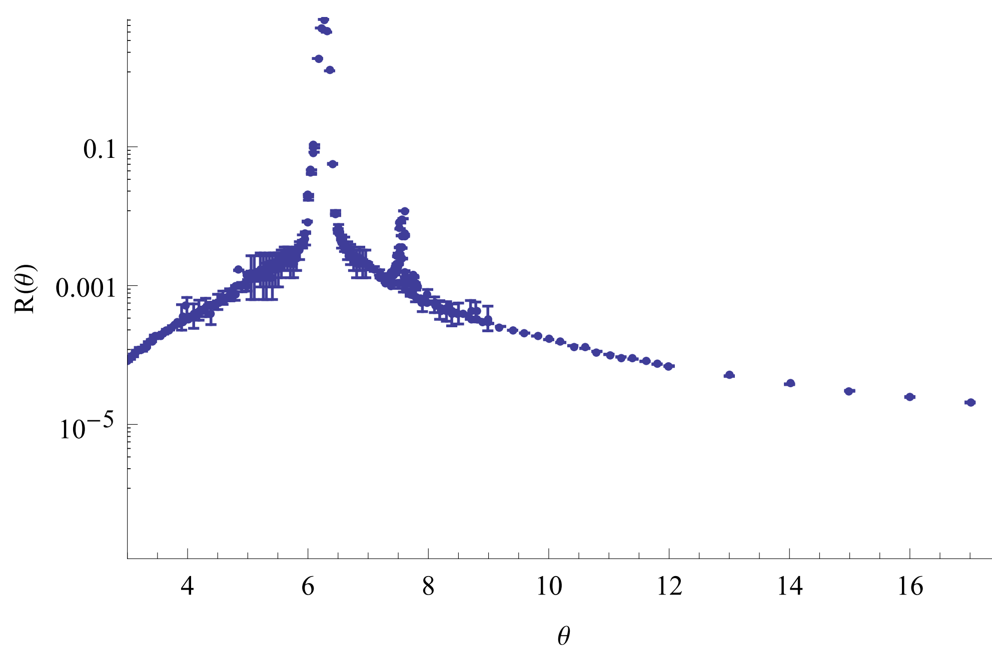

Figure B.3 Reflection per unit angle for uranium oxide sample 2 at 5 nm with a fixed incidence angle of 3 degrees, on a log scale. The curve includes error bars showing statistical error. We were unable to fit the FWHM of the specular peak to any reflectance using Huygens' method.

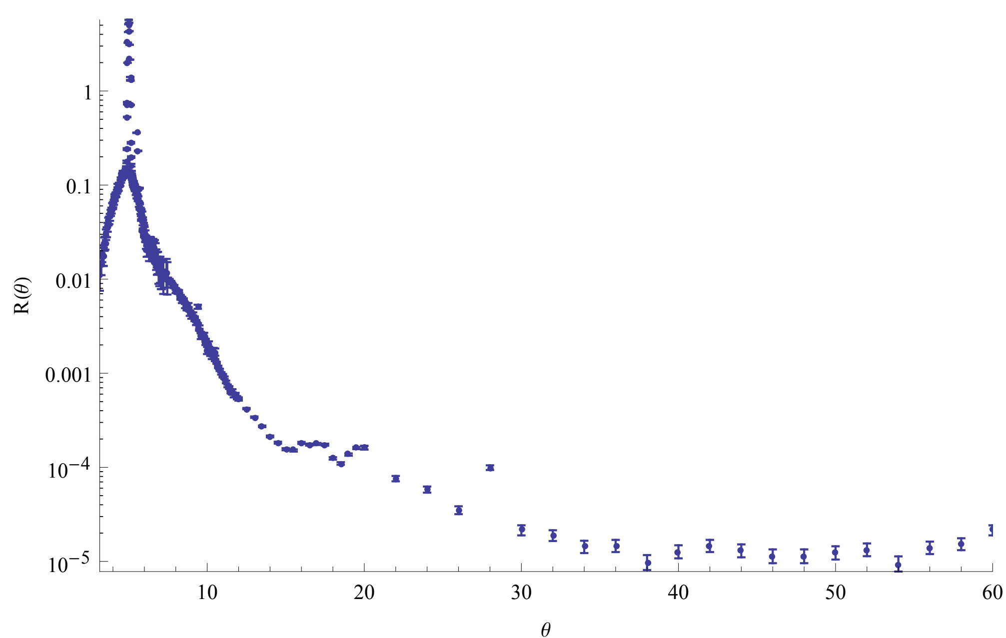

Figure B.4 Reflection per unit angle for uranium oxide sample 3 at 2.5 nm with a fixed incidence angle of 2.5 degrees, on a log scale. Includes error bars showing statistical error. We were unable to fit the FWHM of the specular peak to any reflectance using Huygens' method, nor the sharp decay in the non-specular region.

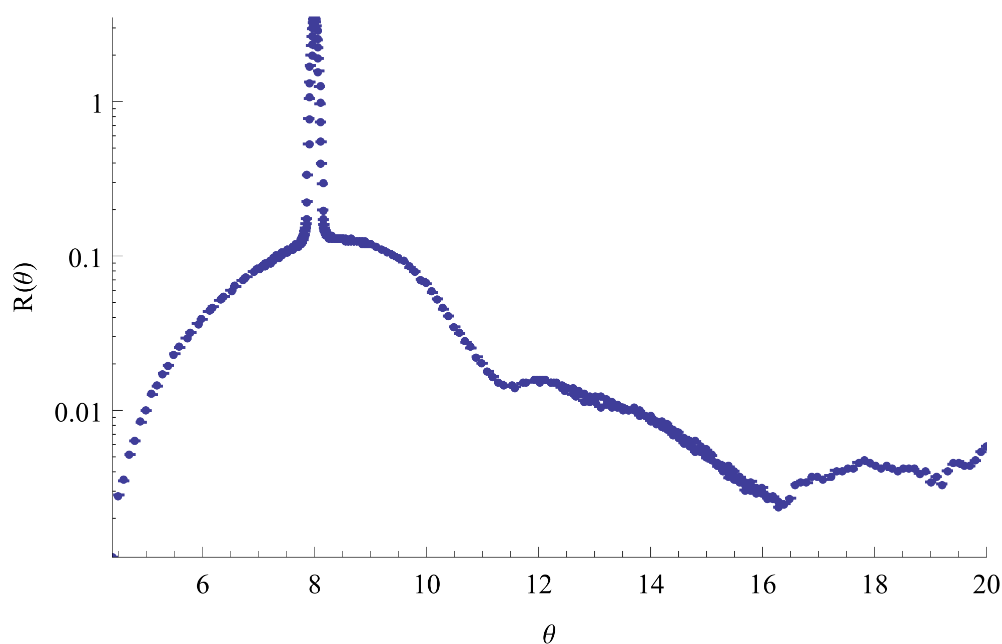

Figure B.5 Reflection per unit angle for uranium oxide sample 3 at 5 nm with a fixed incidence angle of 4 degrees, on a log scale. The curve includes error bars showing statistical error. We were unable to fit the FWHM of the specular peak to any reflectance using Huygens' method, nor the surface features. We were able to fit plateaus using geometrical optics, but we did not fit the rounded decay seen here.

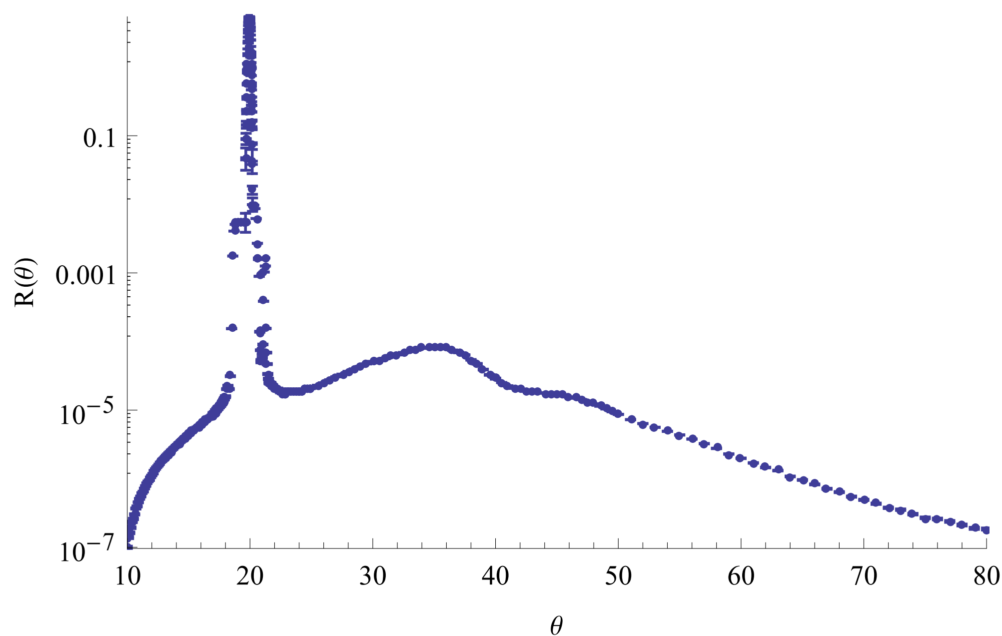

Figure B.6 Reflection per unit angle for uranium oxide sample 30 at 30.4 nm with a fixed incidence angle of 10 degrees, on a log scale. The curve includes error bars showing statistical error. We were unable to fit the FWHM of the specular peak to any reflectance using Huygens' method. We were also unable to fit any of the features using geometrical optics.

Bibliography

[1] J. E. Bjorkholm, “EUV Lithography - The Successor to Optical Lithography,” Intel Technology Journal **Q3,** 1 (1998).

[2] C. Wagner and N. Harned, “EUV lithography: Lithography gets extreme,” Nature Photonics **4,** 24 (2010).

[3] E. G. B.L. Henke and J. Davis, “X-ray interactions: photoabsorption, scattering, transmission, and reflection at E=50-30000 ev, Z=1-92,” Atomic Data and Nuclear Data Tables **54,** 181–342 (1993).

[4] T. F. Marcus Trost, Sven Schroder and A. Duparre, “Influence of the substrate finish and thin film roughness on the optical performance of Mo/Si multilayers,” Applied Optics **50,** C148 (2011).

[5] D. G. Stearns, “The scattering of x rays from nonideal multilayer structures,” J. Appl. Phys. **65,** 491 (1989).

[6] J. E. J. Johnson, “Computationally Modeling the Effects of Surface Roughness on Soft X-Ray Multilayer Reflectors,”, 2006, Masters Thesis.

[7] C. L. Petrie, “Determining thin film roughness with EUV reflection,”, 2014, Senior Thesis.

[8] J. W. Bell, “Thickness Uniformity of Uranium Oxide Films Sputtered While Undergoing Planetary Motion,”, 2013, Senior Thesis.

[9] J. H. Underwood, E. M. Gullikson, M. Koike, P. J. Batson, P. E. Denham, K. D. Franck, R. E. Tackaberry, and W. F. Steele, “Calibration and standards beamline 6.3.2 at the Advanced Light Source,” Rev. Sci. Instrum. **67,** 3373 (1996).